UNLV | UNIVERSITY LIBRARIES

5-1-2024

Remote Detection of Leaks in High Level Waste Storage Tanks

Hunter Frey

Follow this and additional works at: https://digitalscholarship.unlv.edu/thesesdissertations

Part of the Nuclear Engineering Commons

REMOTE DETECTION OF LEAKS IN HIGH LEVEL WASTE STORAGE TANKS

By

Hunter Frey

Bachelor of Science – Mechanical Engineering
University of Nevada, Las Vegas
2022

A thesis submitted in partial fulfillment
of the requirements for the

Master of Science – Materials and Nuclear Engineering

Department of Mechanical Engineering
Howard R. Hughes College of Engineering
The Graduate College

University of Nevada, Las Vegas
May 2024

Thesis Approval

The Graduate College
The University of Nevada, Las Vegas

April 5, 2024

This thesis prepared by

Hunter Frey

entitled

Remote Detection of Leaks in High Level Waste Storage Tanks

is approved in partial fulfillment of the requirements for the degree of

Master of Science – Materials and Nuclear Engineering
Department of Mechanical Engineering

Alexander Barzilov, Ph.D.
Examination Committee Chair

Jeremy Cho, Ph.D.
Examination Committee Member

Charlotta Sanders, Ph.D.
Examination Committee Member

Emma Regentova, Ph.D.
Graduate College Faculty Representative

Alyssa Crittenden, Ph.D.
Vice Provost for Graduate Education &
Dean of the Graduate College

ABSTRACT

The purpose of this research was to characterize three devices potentially capable of remotely detecting signatures of a leak from high-level waste (HLW) storage tanks, specifically ones found at the Savannah River Site and the Hanford Site. The hazard HLW found within these tanks include ^{137}Cs, a gamma-ray emitter, and ^{90}Sr, an electron emitter leading to heat generation. These pose health risks to the personnel and maintenance problems and environmental safety issues if released to the environment. Additionally, pinpointing the location of a leak is a task that could lead to the mitigation of excess waste leaking from the tank.

There were three objectives of this work, each associated with its respective leak detection device. The first objective was to validate a Kromek CZT gamma spectrometer by measuring sealed ^{137}Cs sources with various activity levels. The second objective was to use a FLIR Duo-R thermal camera to image heated metal objects of varying shapes to highlight how a hotspot stands out against a cooler background in thermal imaging. The third and final objective was using a Roga Instruments iSV1611 USB ultrasonic microphone to measure high frequency noises that would be associated with pressurized gas or a liquid leaking from a crack in a tank. Testing each device set a benchmark for accuracy that can be scaled to larger scale experiments and field work.

The experiments completed with these devices provided accurate data used to characterize them to be used in the field. The gamma spectrometer data was compared to known data of ^{137}Cs emissions, and the microphone measured known frequency emissions with extreme accuracy. The thermal camera provided the data numerically, but visually provided great indication of the desired hotspots. The data acquired allowed for a conclusion to be made on the accuracy of these devices to be used to detect a leak in a HLW tank. Future work considered would be large scale experiments and field applications.

ACKNOWLEDGEMENTS

First and foremost, I would like to thank Dr. Alexander Barzilov for his support through this entire process. He was always there to answer questions and assist with anything I needed, and I wouldn't have been able to complete this thesis without him. Additionally, I would like to thank Dr. Jeremy Cho, Dr. Charlotta Sanders, and Dr. Emma Regentova for being my thesis committee members allowing me to present this work.

I would also like to thank my supervisors during my position as an undergraduate Peer Mentor, Shae Deschutter and Dr. Anthony Ferrar. They taught me so much and were instrumental in raising my confidence as not only a student and leader, but as a person as well.

Finally, I would like to give a massive thank you to UNLV as a whole and the UNLV College of Engineering. The professors cared about us students and gave us opportunity to learn and grow ourselves into respectable engineers once we reached the work force. Additionally, the career fairs hosted by UNLV allowed me to obtain my first internship that has now expanded into a full-time position after graduation.

DEDICATION

To my Frey family and the Morejon family, thank you for the unwavering support through this great endeavor.

TABLE OF CONTENTS

LIST OF FIGURES

CHAPTER 1 – INTRODUCTION

1.1 Background

The leakage of high-level nuclear waste (HLW) from storage tanks has been a problem plaguing storage sites for decades. In particular, the tank farms at the Hanford Site (HS) in Washington and Savannah River Site (SRS) in South Carolina are causing problems due to their age. The Hanford site farms contain a total of 177 underground waste storage tanks, with 149 of them being single-shell tanks (SST) and the rest being double-shell tanks (DST). Hanford site began construction of SSTs during World War II to hold the waste from nuclear weapon development. They were only meant to be in use for 20 years, however in the 1950s they started leaking waste into the soil. Consequently, all liquids have been removed from them to reduce the possibility of a leak. Construction started on the DSTs in 1968 to add another layer of leakage protection via an annulus surrounding the tank, thus the "double shell" name. While still in use housing liquid wastes, they are starting to show their age as well [1]. The SRS tank farm contains a total of 51 storage tanks, with only 43 operational. However, many of these are in the process of being cleaned out and shut down due to their aging. As of 2020, the total waste stored at the SRS was 35.6 million gallons, equaling 245 million curies of radiation [2].

The HLW stored in the tanks at Hanford and SRS exist in three forms: sludge, salt cake, and supernatant liquid. The sludge is comprised of water insoluble actinides such as uranium, other transuranic elements, and strontium-90 (^{90}Sr). The salt cake in the tanks was formed via the evaporation of alkaline wastes. The supernatant liquid, a sodium salt enriched liquid, contains cesium, importantly cesium-137 (^{137}Cs) which is highly radioactive [3].

Strontium-90 and Cesium-137 pose major risks if they leak into the environment. Strontium-90, while used in many applications such as medical studies and thermoelectric devices,

is a dangerous unstable isotope if ingested into the body. It is a result of the fission of uranium and plutonium. Sr-90 decays into its daughter yttrium-90, which in turn decays into the stable zirconium isotope. The decays of these isotopes release beta (β) particles with energy levels of 546 keV and 2284 keV respectively. The β-particles emitted interact with the environment, generating high amounts of heat (0.95 W/g). β-particles are able to pass through human skin and can be ingested through food and water. While some will be excreted, the rest is absorbed into the body and is deposited into the bones, increasing the risk of bone cancers and cancer in the tissue near bones [4]. Cesium-137 is similar to Sr-90 in that it is a product of radioactive materials such as uranium and plutonium undergoing fission. It also has its uses in a multitude of areas such as the food industry in food sterilization and medical industry in diagnoses and treatments. While ^{137}Cs also emits β-particles when it decays into its daughter Barium-137m, it also emits dangerous gamma (γ) rays during its lifetime that have an energy level of 662 keV. With no shielding, γ-rays can enter the human body through the skin and ingestion and are distributed throughout the tissues of the body. A 1 μCi ^{137}Cs source will give off a dose of 3.1 mrem/h. While this is low, the activities found in HLW areas will be much higher and could cause much higher doses for workers. While it is expelled over time, the exposure can increase the risk of cancer [5].

The risks associated with these isotopes leaking from the tank farms of Hanford and SRS are why action must be taken to quickly detect leaks and remediate them. Due to the high risks associated, it is not reasonable for a human to personally look for leaks and risk a dose of radiation. Thus, methods of remote detection are preferred. At the tank farms of Hanford and SRS, drones can be equipped with multiple methods of isotope detection to allow for remote detection of possible leaks. While there have been studies with actuating devices to drones, they have been mainly one type such as a radiation detector [6-17]. This work will explore three methods of remote

2

detection that can be actuated to a drone and work in tandem to find any type of leak from a waste storage tank. The methods are gamma-ray measurements using a cadmium-zinc-telluride (CZT) gamma spectrometer, a thermal IR camera, and an ultrasonic microphone. The gamma spectrometer will be able to detect γ-rays emitting from Cs-137, the thermal camera will be able to see the heat generated by Sr-90 decays, and the microphone will be able to hear a leak from a crack in the tank.

1.2 Objectives

The overall objective of this work, characterizing a system of devices capable of detecting a leak from a HLW storage tank, can be broken into three sub-objectives. These sub-objectives are based upon the three devices researched: a CZT gamma spectrometer, an infrared camera, and an ultrasonic microphone. The objectives associated with each are as follows:

1. To positively identify ^{137}Cs sources up to several feet away using a Kromek Gamma Spectrometer within the stated energy resolution of 2.5%. Testing from different distances will show the attenuation due to distance that is important to account for when measuring in the field. Knowing how much distance decreases signature pick-up will help identify small peaks that may arise in field measurements. The spectrometer compiles all the incoming data into a γ-ray spectrum on the computer, displaying it in a readable fashion. The spectrum showcases the γ-ray counts for the sample it is analyzing. Every isotope has its own unique gamma ray signature, so analyzing the spectrometry results will confirm the ^{137}Cs readings are correct [18]. This will prove its reliability for detecting ^{137}Cs, as well as any isotope, in the field.

2. To test a FLIR Duo-R infrared camera utilizing heat sources to sufficiently measure temperature within the +/-5 degrees Celsius range given by FLIR. Temperatures from 10 degrees up to 25 degrees higher than ambient room temperature will be measured to explore the accuracy at higher temperatures. These temperatures will be measured because of the high-heat emission that would be seen at HLW tanks. If a leak occurred, any ^{90}Sr would cause a high temperature change, so measuring distances substantially higher than a few degrees will show the ability of the camera to accurately measure real-world scenarios. Thermal cameras do not see visible light, but instead measure photons in the IR spectrum and therefore measure the heat (energy). They are able to differentiate very small temperature differences and display that difference in various color schemes, depending on user preference [19]. Approximating the temperature a sample of Sr-90 by heating an object to that temperature would allow for a lab test of the IR camera seeing the temperature difference. This would be applicable to looking for Sr-90 leak signatures in the field. Different shapes of metal objects will be imaged to explore the accuracy and resolution of the camera. Heat will move from areas of higher to lower temperature, so the images of the objects will be analyzed to see how the heat distribution is seen in the various shapes.

3. Finally, to test an ultrasonic microphone to positively identify simulated high frequency sounds that would be emitted from air or a liquid leaking out of a pressurized tank. The frequency range that humans are capable of hearing is 20 Hz - 20 kHz [20]. This will be tested using a high frequency emitter and placing the microphone a few feet away from the emitter. Due to some constraints, only frequencies up to 20 kHz can be measured, but the sampling rate will be set to 192 kHz to examine a much large spectrum up to 96 kHz.

CHAPTER 2 – LITERATURE REVIEW

2.1 High-Level Nuclear Waste Generation

During World War II (WWII), the United States (US) was enveloped in the nuclear race against Germany, investing billions of dollars into the project developing the nuclear bomb, the Manhattan Project [21]. Much of this money was put into the development of the uranium and plutonium required for the bombs. The waste byproducts of this generation were eventually stored in large HLW storage tanks, mainly at the HS and SRS. Hanford was the main site for plutonium production, and ended up generating 248 million gallons, or 58% of all nuclear weapon waste produced relating to the Manhattan project [22]. Much of the rest is stored at the SRS, with a small amount also stored at Idaho National Laboratory (INL) and West Valley Demonstration Project located in New York [23]. The total amount of waste stored at HS is about 56 million gallons [24]. Figure 1 shows the total contents of the tank farm at SRS.

The HS in Washington was responsible for the majority of weapons-grade plutonium produced by the US. Weapons grade plutonium, or Plutonium-239 (Pu-239), is created in reactors through Uranium-238 (U-238) undergoing neutron capture. U-238 captures a neutron, producing Uranium-239 (U-239). The U-239 then decays into Neptunium-239 (Np-239), then finally Pu-239, as shown in the nuclear decay chain below [25].

$$^{238}U + n \rightarrow {}^{239}U \rightarrow {}^{239}Np \rightarrow {}^{239}Pu \qquad (1)$$
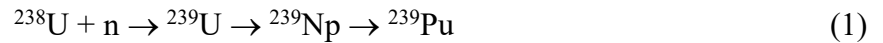
Unlike other uranium isotopes that have half-lives of millions of years, U-239 has a much shorter half-life of about 24 minutes [26]. The half-life of an isotope is the time it takes for half of the atoms present to decay into its daughter isotope [27].

Waste Tank Inventory
Total inventory in 43 waste tanks

Volume

32.9 million gallons (92%)

Salt

2.7 million gallons (8%)

Sludge

35.6 million gallons

Inventory values as of 2020-12-31

Radioactivity

133 million curies (54%)

112 million curies (46%)

245 million curies
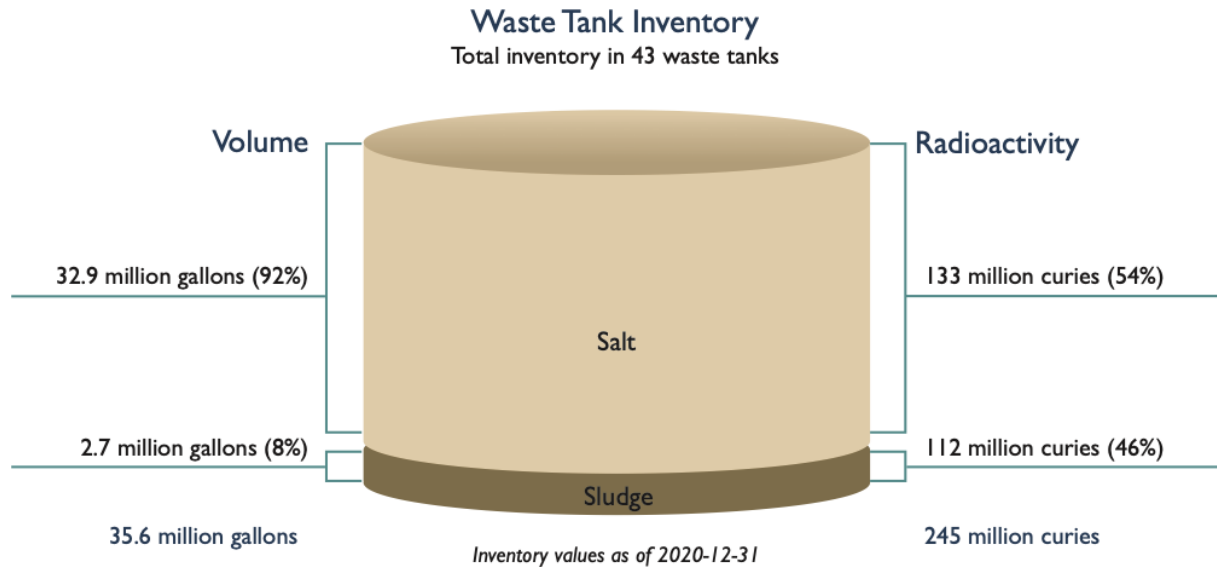
Figure 1: Total HLW Tank Inventory at SRS [2]

Np-239 then has a half-life of 2.4 days before it decays into Pu-239, making the whole decay process only a few days ordeal [28]. Of course, because the Pu-239 is generated in the reactor, it must be separated from the irradiated fuel. Chemical processes allowed for the separation of the plutonium in the form of plutonium nitrate (Pu[NO$_3$]$_4$), which was then sent off to another facility to be converted into the metal plutonium used in nuclear weapon development. All the solutions used in the chemical processes were considered HLW, as they contained uranium and other fission products like Sr-90 and Cs-137 [22]. At SRS, the primary source of waste was the reprocessing of spent nuclear fuel. This included a process named "Purex" that involved separating plutonium from the irradiated uranium fuel [23]. The byproducts of these processes were also considered HLW due to their uranium, Sr-90, and Cs-137 contents and were thus stored in SRS's HLW tanks.

2.2 High-Level Waste Storage

The problem of storing nuclear waste has been a challenge since the very beginning of nuclear waste production. It was known how dangerous radioactive material was and that it must be taken care of. At sites such as HS and SRS, tank farms were designed and constructed as temporary solutions to hold all the HLW they were producing. Unfortunately, many tanks have experienced leaks due to corrosion failures from the harsh HLW within the tanks [23].

At HS, two types of tanks were developed for HLW storage: single-shell and double-shell. The construction of SST was started in 1943 as a quick remedy for the mass amounts of waste resulting from plutonium production for the Manhattan project. Over the next 20 years, 149 SST were built with various volumes, ranging from 55,000 - 1 million gallons (208,000 – 3.8 million liters). They were comprised of welded steel plates placed on underground-molded concrete beds and were then backfilled (essentially buried) 6-12 feet down with only the tops remaining visible [22]. Figure 2 displays the summary of SST built at HS. Figure 3 shows an example of a farm in the process of being backfilled.

Tank Farm	Liner Material	Tanks	Constructed	Initial Operation	Design Life (years)	Present Age (years)
241-B	ASTM A739 (now ASTM A283, Grade D)	16	1943-1944	1945	Not specified	63
241-C	ASTM A739 (now ASTM A283, Grade D)	16	1943-1944	1946	Not specified	63
241-T	ASTM A739 (now ASTM A283, Grade D)	16	1943-1944	1944	Not specified	63
241-U	ASTM A739 (now ASTM A283, Grade D)	16	1943-1944	1946	Not specified	63
241-BX	ASTM A739 (now ASTM A283, Grade D)	12	1946-1947	1948	Not specified	60
241-TX	ASTM A285-46 (Grade unknown)	18	1947-1948	1949	Not specified	59
241-BY	ASTM A283-46T or A285-46 (Grades A, B, or C)[7]	12	1948-1949	1950	Not specified	58
241-S	ASTM A283-46T (Grade B)[8]	12	1950-1951	1952	Not specified	56
241-TY	ASTM A283-49T (Grade B)[9]	6	1951-1952	1953	Not specified	55
241-SX	ASTM A283-52T (Grade Unknown)	15	1953-1954	1954	Not specified	53
241-A	ASTM A283-52T or A285-52aT (Grade Unknown)	6	1954-1955	1956	Not specified	52
241-AX	ASTM A201-61T, Grade A	4	1963-1964	1965	25	43

Figure 2: Summary of SST tank farms at Hanford site. "Present Age" is as of 2009 [22].

Figure 3: Hanford site tank farm 241-TX being backfilled [22].

As of 2009, over 67 of the 149 SST at HS were either confirmed to have leaked waste or were assumed to have leaked waste [22]. Since then, more SST have started leaking HLW into the surrounding soil [29]. The largest leak occurred in 1973 and was recorded to be 115,000 gallons (435,000 liters). In total, approximately 1 million gallons had leaked by 2009. Research was conducted in the 1970s as to why the SST were leaking, especially before their expected lifetime age. It was found that the high concentration of sodium nitrate stored in the tanks were causing corrosive cracks in the steel walls [30]. While there were chemical controls put in place to maintain a basic pH of around 10 in the tanks, no controls were setup to reduce corrosion on the inner walls or workings of the SST. Once a leak was detected, however, the liquid waste in the leaking tank was then pumped to either another SST, or if the leak occurred after 1968, to a DST.

In 1968, HS began construction on DST due to the SST reaching their capacity. Plutonium production was still continuously happening, and thus more tanks needed to be built. Hanford site scientists and engineers learned from the mistakes of the SST and built the more secure DST, improving the design and adding more safety features.

DST are essentially a tank within a tank. The inner steel tank is similar to SST but it is also surrounded with an outer steel liner made of various types of steel as shown in Figure 4. This acts as a catch for anything that may leak out of the inner tank. Anything leaking into the outer liner will be geometrically directed into a leak detection pit. These new tanks are similar in size to the larger SST, being able to hold 1.1 million gallons (4.2 million liters) of HLW [22]. Figure 5 shows a DST farm nearing completion. In addition to having the outer liner, DST were also stress-relief annealed to relieve internal stresses within the tank walls [30]. The tanks were constructed from welded steel, and when a metal like steel is welded, it undergoes thermal expansion and

9

contraction. This heating and cooling introduce stresses in the metal that can lead to corrosion cracking [31]. The annealing process relieves those internal stresses, making the metal more resistant to cracking. Cathodic protection was also added to the DST to help prevent corrosion cracking [22].

Tank Farm	Liner Material	Number of Tanks	Construction Period	Initial Operation	Service Life (years)	Current Age (years)
241-AY	ASTM A515, GR 60	2	1968-1970	1971	40	37
241-AZ	ASTM A515, GR 60	2	1971-1976	1976	20	31
241-SY	ASTM A516, GR 60	3	1974-1977	1977	50	30
241-AW	ASTM A537, CL1	6	1976-1980	1980	50	27
241-AN	ASTM A537, CL1	7	1977-1979	1981	50	28
241-AP	ASTM A515, CL1	8	1982-1986	1986	50	21

Figure 4: Summary of DST at Hanford Site. "Current Age" is as of 2009 [22].

Figure 5: Hanford Site DST farm 241-AP nearing backfill completion [22].

While there are still problems with SST leaking HLW [29], there are no current leaking problems with the DST. Thanks to the metal treatments of annealing and cathodic protection and additional risers for accessing and testing the tanks, the DST have not provided much problem. However, with some of the farms either exceeded or reaching their service life, it is only a matter of time before a problem arises and the need for leak detection systems for quick remediation are required.

The HLW tanks at SRS first started construction in the 1950s. Whereas HS has two different types of tanks with SST and DST, SRS has four types of tanks: Type I, Type II, Type III, and Type IV. The first Type I tanks were built in 1952, and over the next 30 years, 51 tanks of various types were built. Figure 6 summarizes the tanks built and their materials [23].

Tank no.	Type	Year built	Material of construction for primary tank	Steel design code
1F–8F	I	1952	A285 Grade B	ASME BPV-1949
9H–12H	I	1953	A285 Grade B	ASME BPV-1949
13H–16H	II	1956	A285 Grade B	ASME BPV-1952
17F–20F	IV	1958	A285 Grade B	ASME BPV-1956
21H–24H		1962	A212-57T Grade B	
25F–28F	III	1975–1978	A516 Grade 70 (N)	ASME BPV-1956 or 1965
29H–32H		1967–1970	A516 Grade 70	as appropriate
33F–34F		1969–1972	A516 Grade 70	
35H–37H		1974–1977	A516 Grade 70 (N)	
38H–43H		1976–1980	A537 Class I (N)	
44F–47F		1977–1980	A537 Class I (N)	
48H–51H		1978–1981	A537 Class I (N)	

Figure 6: Summary of HLW tanks built at Savannah River Site [23].

There were 12 Type I tanks built between 1952 and 1953 as Figure 6 displays. These tanks were large underground tanks with a capacity of 750,000 gallons (2.8 million liters). They were built of steel surrounded by an annulus and a concrete encasement as shown in figure 7. Like the SST at HS, the metal the Type I tanks were made of were not annealed and therefore suffered from corrosion stress cracking. In just the first two years of their existence, four tanks started leaking.
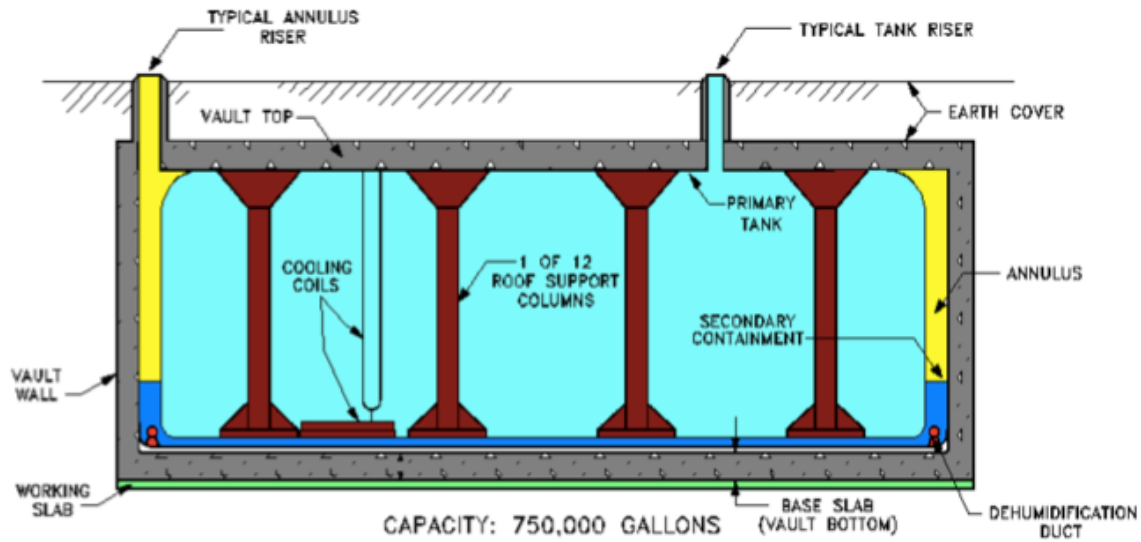
Figure 7: Savannah River Site Type I tank design [23].

The largest leak recorded was tank 16H which experienced a 185,000-gallon (700,000-liter) leak. One of the major design flaws of the type I tanks was the temperature limit. The tank was designed for temperatures around 100 degrees Celsius, but the sludge waste in the tanks containing the hot Sr-90 reached temperatures of up to 350 degrees Celsius [23]. As of 2021, there were no leak sites in these type I tanks and the waste still stored in them is kept at a level below previously known leak locations [2,23].

Only a few years after the type I tanks were built, the type II tanks were constructed. Four were constructed, one of which being tank 16H which experienced the largest leak and had 145 leak sites identified between 1961-1962 [23]. Figure 8 shows the design of the type II tanks. Type II tanks were larger than type I tanks with a capacity of 1.03 million gallons (3.9 million liters). These were similar to type I tanks in terms of materials and design. Steel plates were welded

13

together to create the inner tank and outer catch. It was also surrounded in a concrete vault. The main internal difference between a type I and type II tank was instead of being constructed with multiple smaller support columns like shown in figure 7, type II tanks were built with a large singular center support column. Like the type I tanks, type II tanks were not annealed to reduce the internal stresses to help prevent cracking, leading to leaks [23]. Due to the temperature design flaw of tank I, tank II was designed with proper temperature limits, able to withstand temperatures up to 400 degrees Celsius. As of 2021, one tank had been shut down and grouted, while the other 3 still hold waste held at levels below the known leak locations [2].

The jump from type II to type III tanks was a large one with many improvements. Figure 9 displays the type III tank design, which right away can be compared to the type II tank design. The designs are very similar, but type III tanks have improvements such as a full size secondary
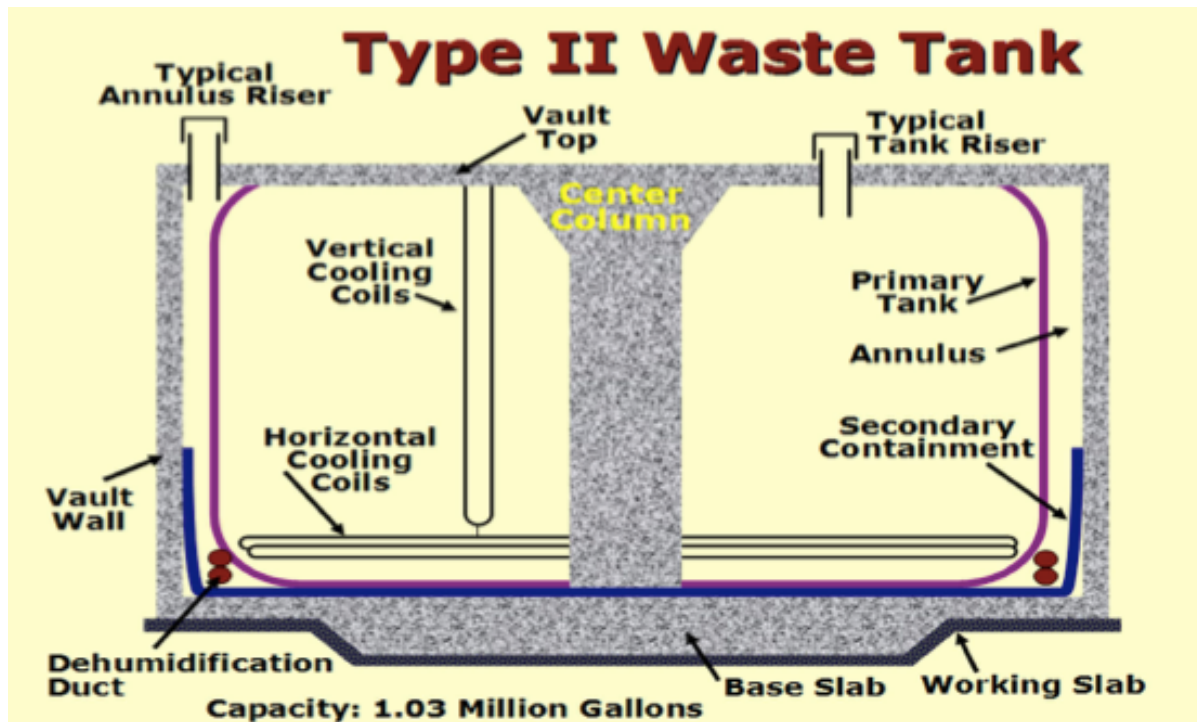
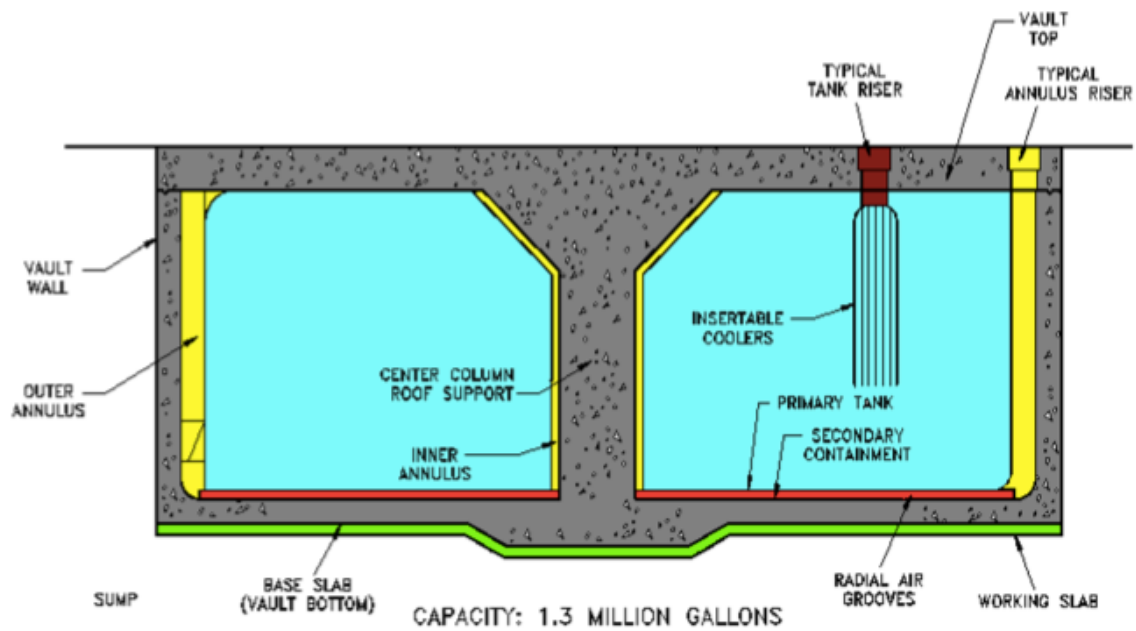Figure 8: Savannah River Site Type II tank design [23].

Figure 9: Savannah River Site Type III tank design [23].

tank and an inner and outer annulus. Type III tanks again had their volumetric capacity increased up to 1.3 million gallons (4.9 million liters). In addition to capacity, the number of tanks built was increased as well. Whereas only 16 tanks total were built of type I and type II tanks, 27 type III tanks were built [2,23]. Possibly the most important feature added to type III tanks was adding the annealing process to the construction of the tank. The lack of annealing in type I and type II tanks led to more corrosion cracking and thus leaks. This is the same problem HS experienced with their SST, leading to annealing being added to the construction process of DST. Thanks to this stress-relieving process, none of the type III tanks, which hold a vast majority of the waste stored at SRS, have leaked [2].

The remaining tanks at SRS are type IV tanks. These are different from the other types in terms of the kind of waste they hold. Though they weren't built to handle the hot HLW, that is what type I held, and types II and III were then fixed to be able to withstand the high temperatures. Type IV, on the other hand, were built to store the lower temperature waste under 100 degrees Celsius. Type IV tanks have the same capacity as type III tanks (1.3 million gallons or 4.9 million liters) and were also made of steel and concrete but had a dome top instead of flat. Type IV tanks also did not have a secondary containment area for leaks as shown in figure 10. While the steel in these tanks were not annealed to reduce internal stresses, the second batch built in 1962 were made of a different steel, A212, as shown in figure 6. The first batch of type IV tanks built in 1958 were constructed using the same steel as type I and II tanks, and thus suffered from cracks and leaks [23,32]. Four of the eight type IV tanks built have been shut down and grouted, while the other four are still holding waste and have not leaked [2]. The A212 steel used in the second batch of type IV tanks was not only annealed to reduce the internal stress, but also contained a carbon content of 0.18 wt%, making it more resistant to stress-corrosion cracking [23].

16
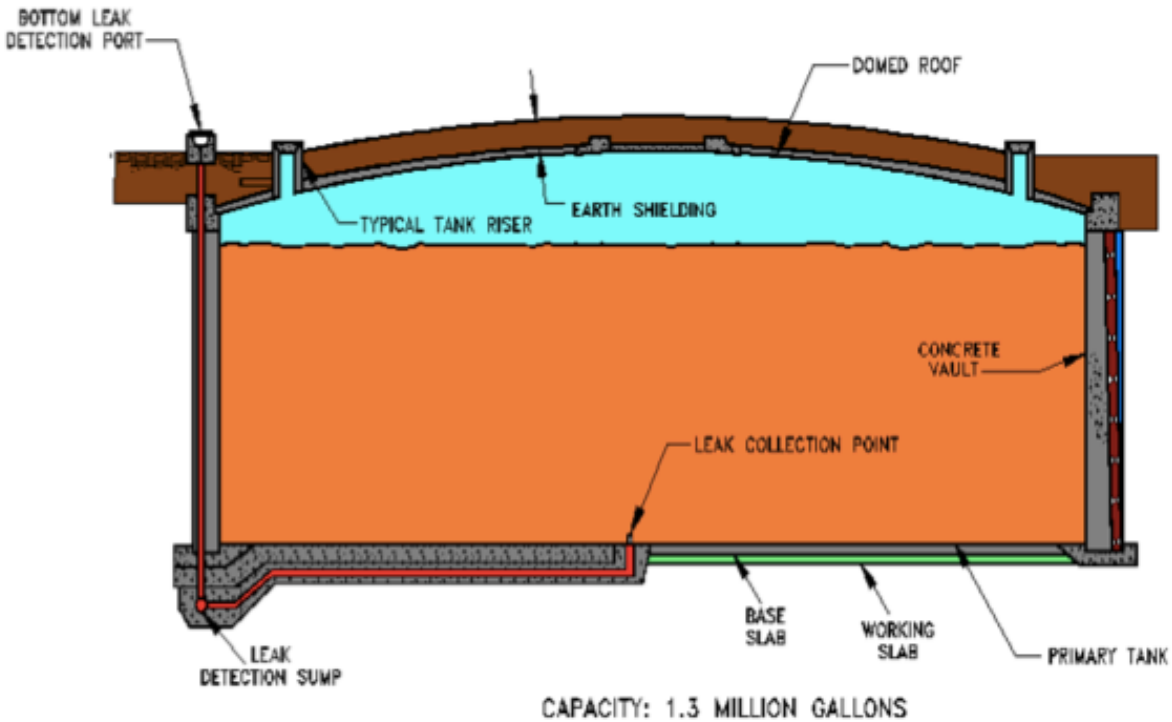
Figure 10: Savannah River Site Type IV tank design [23].

2.3 Radiation

One of the main topics in the nuclear engineering field is radiation. Radiation is involved in many different fields from medical, to transportation of waste, to the operation of a nuclear reactor. Detectors are essential in maintaining the levels of radiation allowed in a certain area. This applies to the waste storage tanks at HS and SRS where leaks are occurring. The quick and accurate detection of a Cs-137 is required to remediate a leak safely and efficiently.

There are different types of radiation emitted depending on the material or element. The different types of radiation emitted from radionuclides are alpha (α) particles, beta (β) particles,

neutrons, and gamma (γ) rays. These are emitted in different ways depending on the radionuclide. ^{137}Cs naturally emits γ-rays, but also emits β-particles when it decays into its daughter ^{137}Ba [33].

An α-particle consists of two protons and two neutrons, making it the heaviest form of radiation and equivalent atomically to the nucleus of a helium atom. These particles are often emitted by the naturally occurring radioactive elements on earth [34,35]. While α-particles are dangerous if ingested by the human body, it is very easy to shield against them. They cannot pass through even a piece of paper, much less human skin [34,36].

A β-particle is essentially just an electron. However, it is unique in that it can either be positively or negatively charged, depending on the kind that is emitted. A negatively charged β-particle is identical to an electron, whereas a positively charged β-particle is identical to a positron, which is a positively charged electron. These particles are also easy to shield against, as something like a thin sheet of metal will stop them [37]. Most elements that emit β-particles also emit gamma rays, like ^{137}Cs, but there are also pure β emitters like ^{90}Sr [36].

Neutrons are different from the other types of radiation in that they are not emitted naturally from materials [35]. Neutrons are commonly emitted when a heavy element, such as uranium, undergoes fission. They are incredibly important in fission because nuclear chain reactions can only be sustained with sufficient neutron production [34]. There are multiple different names for neutrons depending on their energy level. Neutrons with energy levels between 0-0.025 electron-volts (eV) are known as cold neutrons. A neutron with an energy of 0.025 eV is known as a thermal neutron and is particularly interesting in that a neutron with that energy is at equilibrium with the motion of the medium it is found. Epithermal neutrons are neutrons within the energy range of 0.025 to a few hundred eV. The next group, slow neutrons, are between a few hundred eV and

about 0.5 MeV. Neutrons between 0.5-20 MeV are known as fast neutrons. Finally, a neutron above 20 MeV is known as a high energy neutron [38].

A γ-ray is a form of electromagnetic radiation. It is able to easily penetrate the human body unless there is heavy shielding present. This is helpful when it comes to medical purposes such as cancer treatment, but in high doses can be fatal. The γ-rays emitted require a highly dense materials such as lead to stop it, and even then, some of the rays can bleed through. Figure 11 is a simple diagram showcasing the shielding sufficient for each type of radiation [34,36].
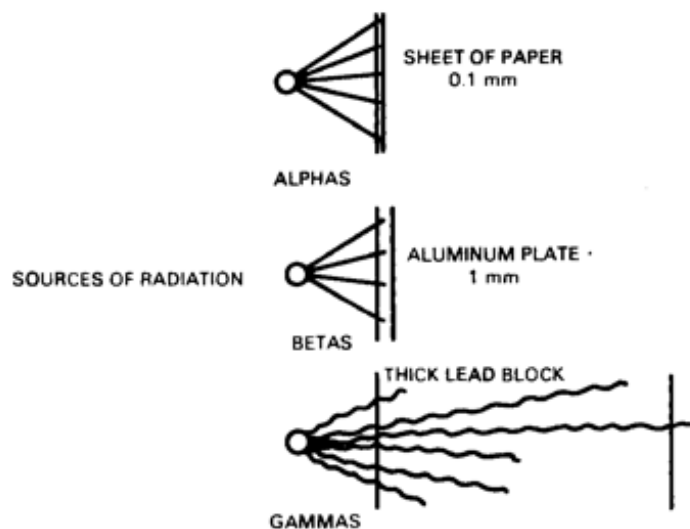

Figure 11: Diagram showcasing the shielding of different types of radiation [35].

The danger of radiation requires the capability to be able to detect it and quantify it. There are various devices that have been used over time to detect the different kinds of radiation [39]. Today, the newest devices used in detection of gamma rays and neutrons are semiconductor detectors. These detectors include scintillators, crystals used to detect radiation, and CZT detectors, which have the advantage of not requiring cryogenic cooling to be used. Instead, they can be used in ambient temperature conditions.

2.4 Radiation Detectors

Scintillators are clear elpasolite crystals grown for the specific reason of detecting ionizing radiation such as γ-rays and neutrons. In fact, many are dual γ/n detectors capable of detecting both at the same time. There are multiple different kinds of scintillators with different chemical properties. They include CLLBC ($Cs_2LiLa(Br_6)_{90\%}(Cl_6)_{10\%}$) doped with Ce^{3+} and CLYC (Cs_2LiYCl_6) which can be enriched with either ^6Li or ^7Li depending on the desired application. Scintillators utilize photo-multiplier tubes (PMT) to generate signals suitable to create the spectrum used for analysis. Certain isotopes are used for different energy levels of neutrons wanting to be measured. For example, ^3He and ^{10}B have high neutrons total cross sections for low-energy slow thermal neutrons. Then there is Cl, which is more effective at absorbing fast energy neutrons [40]. These scintillators have many lab and field applications that can be utilized in a variety of disciplines [41-50].

Scintillators work in tandem with PMTs in gamma detection. When ionizing radiation interacts with scintillators, they emit photons of different wavelengths depending on the scintillator properties, as shown in figure 12. The photons emitted from the scintillator than travel into the PMT and, which utilizes the photoelectric effect to generate a signal. The PMT includes a photocathode that experiences the photoelectric effect. When a photon emitted by the scintillator

enters the photocathodes, the photoelectric effect causes the photon to completely transfer its energy to an electron within the material, which is then ejected. This electron then enters the multiplying area of the PMT, an area comprised of carefully placed dynodes. When an electron collides with a dynode, it emits secondary electrons. These electrons are accelerated towards the next dynode which has a higher electric potential. At each subsequent dynode, more and more secondary electrons are emitted, eventually amplifying the signal thousands or even a million times. This current can then be analyzed to determine the energy of the original radiation particle that entered the scintillator [51].

Figure 12: Scintillators illuminated with different wavelengths of color [52].

CLYC (Cs_2LiYCl_6:CE) is a scintillator capable of gamma and neutron detection. The standard one is Li_6 enriched and is used as a thermal neutron scintillator. Thermal neutrons are neutrons with energies between 0.02 and 10 eV. It is sensitive to thermal neutrons from the $^6Li(n,\alpha)t$ reaction. Spectroscopy can then be analyzed to obtain the FWHM (full width half maximum) and timing resolution [53].

C^7LYC scintillators are CLYC crystals enriched with ^7Li. Where normal CLYC crystals with ^6Li are used due to the enhanced thermal neutron efficiency, C^7LYC crystals suppress the thermal neutron response, allowing for improved neutron spectroscopic capabilities. Suppressing the thermal neutron response allows for detection of fast neutrons (>1 MeV) to not be blocked by thermal neutrons. This means the spectroscopy can be observed in a region previously obstructed by the thermal neutron peak. PSD plots can be created for different neutron energy level measurements to explore the detector response and peak structure. The main peak in the pulse-height spectra is due to the $^{35}Cl(n,p)^{35}S$ reaction. As the energy increases, the structure follows the path of single peak to double peak to a continuum. Once the continuum is reached, the main peak is lost [54]. In these CLYC scintillators, pulse shape discrimination (PSD) is performed to separately identify the neutron and gamma peaks in the spectroscopy.

Pulse Shape Discrimination is a ratio defined as the ratio between long and short time windows. These are to each other, for example [55] has Q_{long} as a 800 ns window and Q_{short} as a 100 ns window. The decay times for gamma rays and neutrons are different, so the PSD ratios for each will differ. These different ratios will manifest themselves in the data, allowing for the separation of gamma ray and neutron spectrums [55].

CLLBC is a scintillator that also doubles as a neutron and gamma ray detector. Because of its higher photon yield, CLLBC has higher gamma ray detection efficiency and better energy resolution than CLYC crystals. However, unlike CLYC crystals, CLLBC can measure thermal and fast neutrons, as well as alpha particles. Alpha particles, thermal neutrons, and gamma rays are easily separated, but a problem with fast neutrons arises in the bromine contents of the crystal. The fast neutrons can cause the Li, Br, and La within the crystal to emit protons, deuterons, tritons, or more alpha particles. These particles will all elicit a response in the spectra. Because of this, the discrimination between gamma rays and fast neutrons is not as easy as thermal neutrons [56-62].

When it comes to radiation detection, there are 2 types: active and passive assay. Active assay utilizes an external radiation probe to induce a response of an analyzed object. Fissile and fertile isotopes spontaneously emit neutrons and γ-rays which then irradiate the target object. Certain nuclear materials can fission from this irradiation, emitting their own neutrons and γ-rays. These are emitted immediately, known as prompt fission radiations, and for several minutes following fission, known as delayed fission radiations. Something to take into consideration is distinguishing the fission neutrons and γ-rays from the source irradiation neutrons and γ-rays. Passive assay, on the other hand, allows for remote detection of neutrons and γ-rays emitted from spontaneously decaying nuclear materials. Issues with passive assay include radiation with a low enough energy to be easily shielded and background radiation causing noise. Thankfully, modern systems are able to eliminate much of this background radiation, improving detection quality.

Another crystal used in gamma ray detection is CZT. CZT detectors have a bandgap, or amount of energy needed to excite an electron, ranging from 1.5 to 2.2 eV. This is considered a high bandgap, also known as a wide bandgap. This value ranges depending on the concentration of Zinc (Zn) present in the compound. In the early times of CZT usage, the measurable energy

range was limited to 200 keV. This was due to the inability produce crystals larger than a few millimeters and poor hole mobility [63,64]. A hole, or an electron hole, is the lack of an electron left in the valence band when it moves to the conduction band, which is a common occurrence in semiconductors like CZT [65]. However, advances in crystal growth technology have led to the modern CZT detectors capable of being several cubic centimeters in volume. These large crystals being grown can detect photons with energy levels up to 2 MeV. This higher energy range of measurement capability combined with room temperature operation make CZT detectors a viable option for field application.

A CZT gamma spectrometer has the advantage of being a room temperature operable detector and easily packed into a field ready device, but also has the disadvantage of being small. This means the counting of γ-rays will be lower compared to other scintillator crystals, so the CZT needs more time to gather enough data to be accurate. While the CZT crystals can be grown larger to detect high energy photons more easily, most commercially available ones, such as the Kromek CZT detector used in this work, are smaller. This limits good resolution to energy levels around 600 keV. While higher energy photons will still be detected and visible in the created spectrum, it would take more time for them to appear [66]. This may present a problem if the detector is used in a constant motion, such as on a drone or robot. Once the spectrum is created via software, it can be analyzed to determine/verify the isotope being measured. Isotopes that emit gamma-rays do so with a characteristic energy level, such as ^{137}Cs emitting a 662 keV gamma-ray. Comparing the peaks found in a spectrum to known energy levels determines the isotope being measured.

CHAPTER 3 – METHODOLOGY

3.1 Methodology

The purpose of the experiments done in support of this work is to test the devices to verify that they could be applied in the field to remotely detect leaks from HLW tanks via the three leak's signatures. A CZT detector, a FLIR Duo-R thermal camera, and an ultrasonic microphone were used to perform the necessary experiments. The data acquired was analyzed for accuracy to determine whether the devices could be used remotely to detect leaks in a HLW tank. The gamma spectra from the CZT detector were analyzed to look at the resolution and range fall off thanks to the inverse square law. The thermal camera was used to take pictures and record a hot spot relative to its surroundings to show how a leak would be seen in the IR spectrum. Finally, the ultrasonic microphone was used to "listen" to a medium flowing out of a small, pressurized tank simulating the real HLW tanks at the tank farms at SRS and HS.

3.2 CZT Gamma Spectrometry

The radiation detection system used to measure γ-rays was a Kromek GR1-A+ CZT gamma spectrometer. This detector contains a 1 cm x 1 cm x 1 cm cubic CZT crystal used in the detection process. It has everything contained within, including a preamplifier, and transmits the data to a computer via USB. The stated energy resolution, the ratio between FWHM and peak centroid, this detector according to Kromek is <2.0% [66]. The free software from Kromek, KSpect, was used to analyze the data. KSpect automatically creates the γ-ray spectrum from the data and updates it live. An example spectrum of just background radiation (radiation detected from the environment) is shown in Figure 13. The x-axis is the bin number, or energy level. The y-axis is the counts, or

number of γ-rays being detected. Before taking measurements, the CZT detector had to be calibrated.
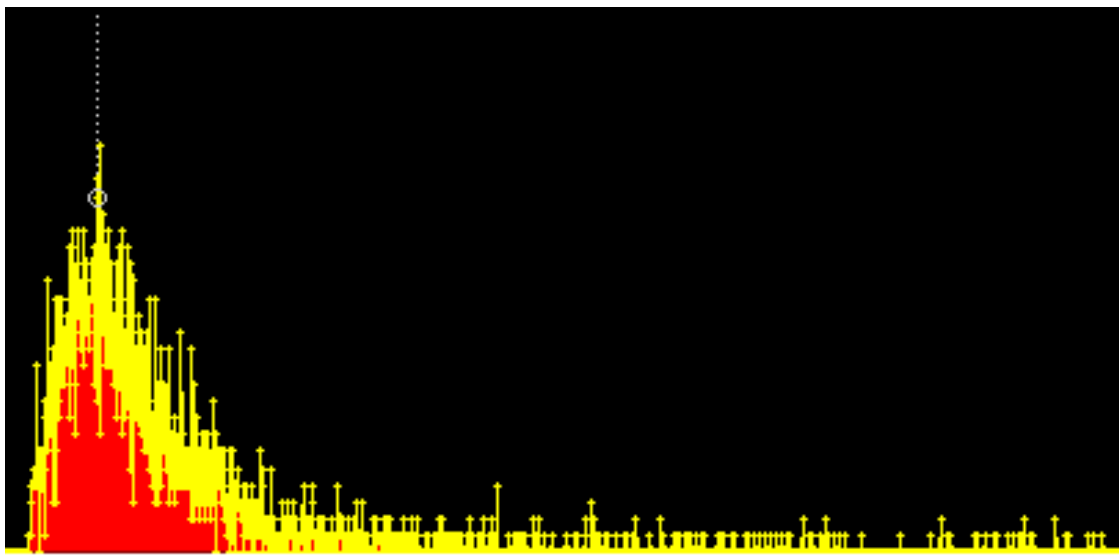

Figure 13: A test spectrum created via the KSpect software showing background radiation.

To calibrate the detector, three sealed radioactive sources were used. These include ^{137}Cs, ^{22}Na, and ^{60}Co. Before calibration, the spectrum created in KSpect just has the bin, or channel value on the x-axis. These three isotopes were measured, revealing peaks in the spectrum. The peak is a gaussian distribution about the known energy value. The known energy values, shown in Table 1, were used in a linear calibration inside the KSpect software. Remeasuring only ^{137}Cs and seeing the peak around 662 keV confirmed the calibration was done correctly. Since the main threat of γ-ray exposure from the real life HLW tanks comes from the ^{137}Cs within them, it is

advantageous to do complete experiments with the same isotope. Two different sealed ^{137}Cs sources were measured for 1 hour from various distances with the CZT detector. They had activities of 0.898 μCi and 16 μCi respectively when calibrated in 2011, but with the decay occurring since, now have activities of 0.675 μCi and 11.94 μCi respectively. For simplicity, these are referred to as "0.898 μCi" and "16 μCi" respectively. The results of these experiments were expected to show the high energy resolution of the CZT detector and accurate measurements of the 662 keV γ-rays emitted by ^{137}Cs.

Isotope	Gamma-ray Energy Level[s] (keV)
^{137}Cs	662
^{133}Ba	356
^{60}Co	1173, 1332

Table 1: Isotopes used in the CZT detector calibration [33].

During experimentation, the radiation safety principle, "as low as reasonably achievable," or ALARA, was followed. First, a dosimeter was worn at all times while conducting experiments with the radiation sources. The sources were held radially to limit the direct exposure of touching the point source location. Additionally, once the sources were placed in their respective spot for experimentation, all humans stayed a sufficient distance away where the computers were located.

Finally, sources were immediately returned to their packaging in the radiation vault in the lab once experimentation was complete. These precautions limited the radiation dose received to the lowest possible amount, correctly following ALARA.

3.3 Infrared Optics

Another problem the HLW tanks are experiencing when they leak is heat. The ^{90}Sr in the sludge in the tanks is a high heat emitter, so if a crack and thus leak occurs near the areas where there is sludge, the heat will be emitted to the environment. This is where an infrared (thermal) camera would be useful. To test the capability of this idea, a FLIR Duo-R thermal camera was used to record and take pictures of heated objects in the lab. To prove the concept of the camera being able to "see" a hotspot, an object was heated to a temperature higher than the surroundings through the use of a heating tape. Utilizing a portable screen attached to the camera via micro-HDMI, the camera was used to measure the temperature of the heated object. According to FLIR, this camera has a temperature accuracy is +/- 5°C [67]. The camera was set to a red/orange/blue color setting through the FLIR UAS app downloaded onto an iPad. This made the "cold" spots blue and "hot" spots a red/orange color. This stark color contrast made viewing the hotspot easy. In addition to color, a greyscale could also be used. The accuracy of the camera was verified using a K-type single channel thermocouple to directly measure the temperature of the object.

3.4 Ultrasonic Signatures

It is common to hear a high pitched-whistling sound when, for example, and air pipe cracks and the pressurized air is being released into the environment. This same concept applies to a crack in the pressurized HLW tanks. However, if there is a micro-crack, the frequency may be too high for the human ear to hear. Thus, an ultrasonic microphone could be used to "hear" in the higher frequency ranges. To test this, an ultrasonic microphone from Roga Instruments was used. This microphone contained a calibrator, making calibration much simpler. Initial tests were run with a high frequency sound emitter app on a phone. This allowed for measurements of known frequencies to test for accuracy. A small tank simulating the HLW tanks found in the tanks farms at SRS and HS was machined by the UNLV Machine Shop for use in this experiment, as shown in the drawings in Figure 14. The tank has interchangeably sized drilled holes to emulate cracks to test the range of the microphone. An air compressor was used to pump air through the tank and the "crack," and the microphone was used to listen to any higher frequency sounds emitted during the process.
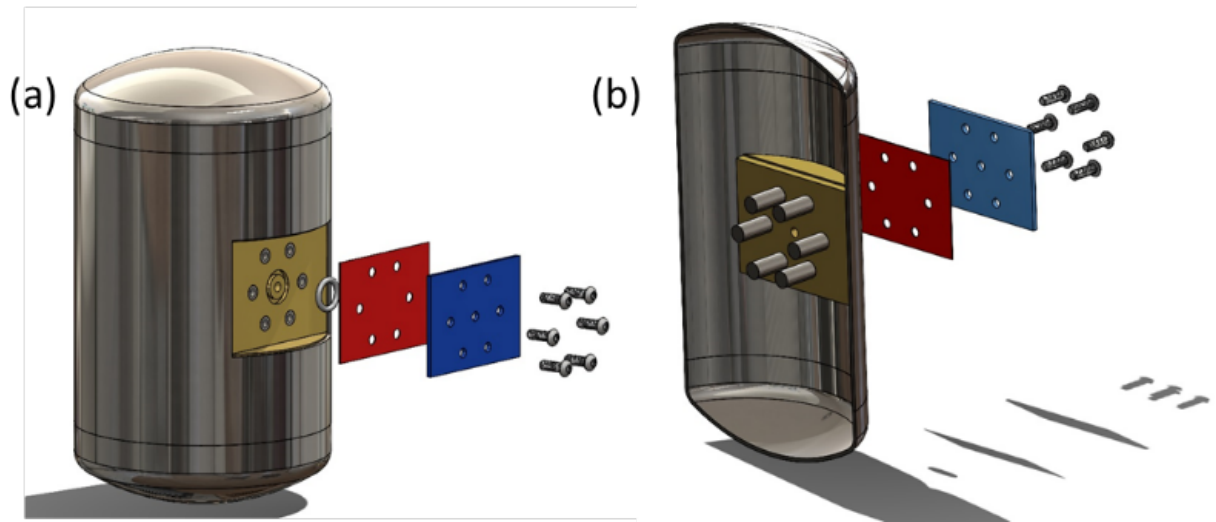
Figure 14: Drawing of the machined tank simulating the HLW tanks found at SRS and HS. Includes the interchangeable plates with varying hole sizes to imitate differing crack sizes. Can be used for ultrasonic testing or leaking liquids.

CHAPTER 4 – RESULTS & DISCUSSION

4.1 Gamma Spectrometry

The CZT spectrometer measured the sealed ^{137}Cs sources for 1 hour from varying distances. Both the 0.898 µCi and 16 µCi sources were measured to examine the differing attenuation through air from different activity levels. The following figures show the γ-ray spectra created in KSpect. In addition to the spectra, the associated gaussian distributions are also displayed in the following figures.
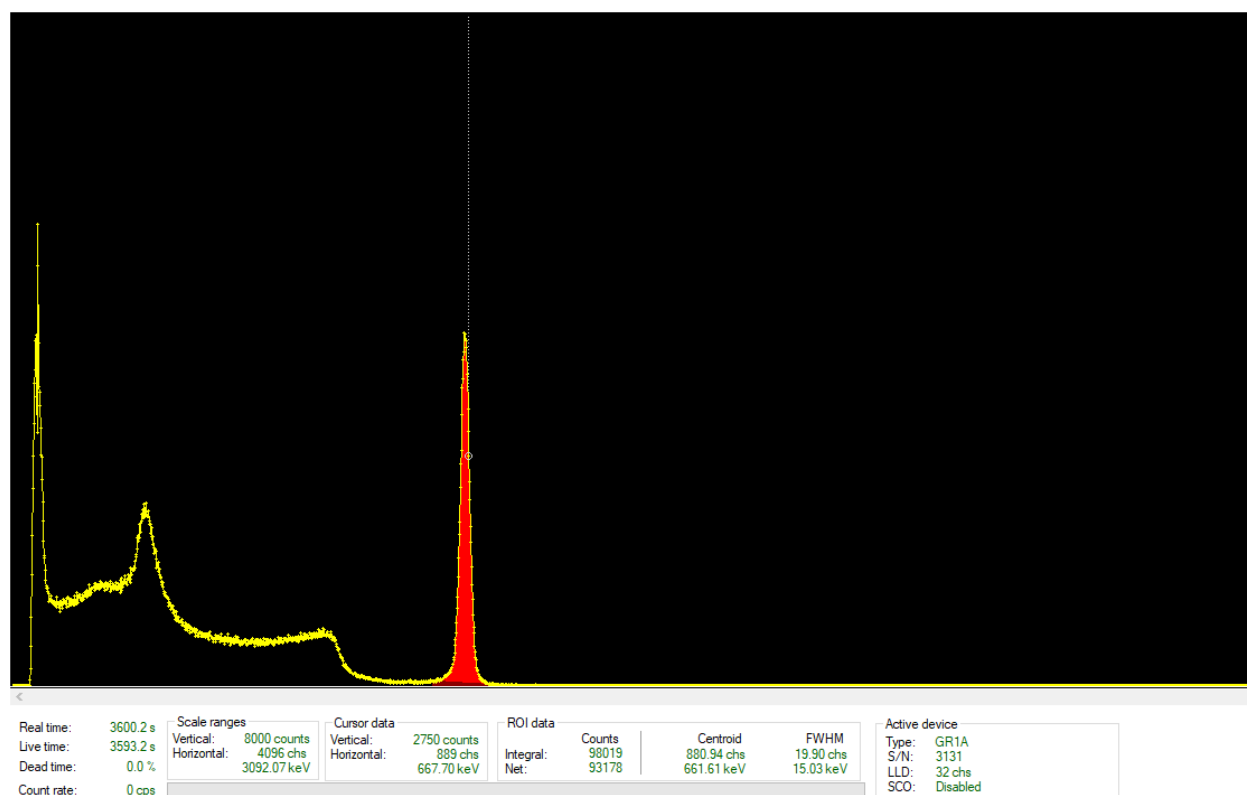

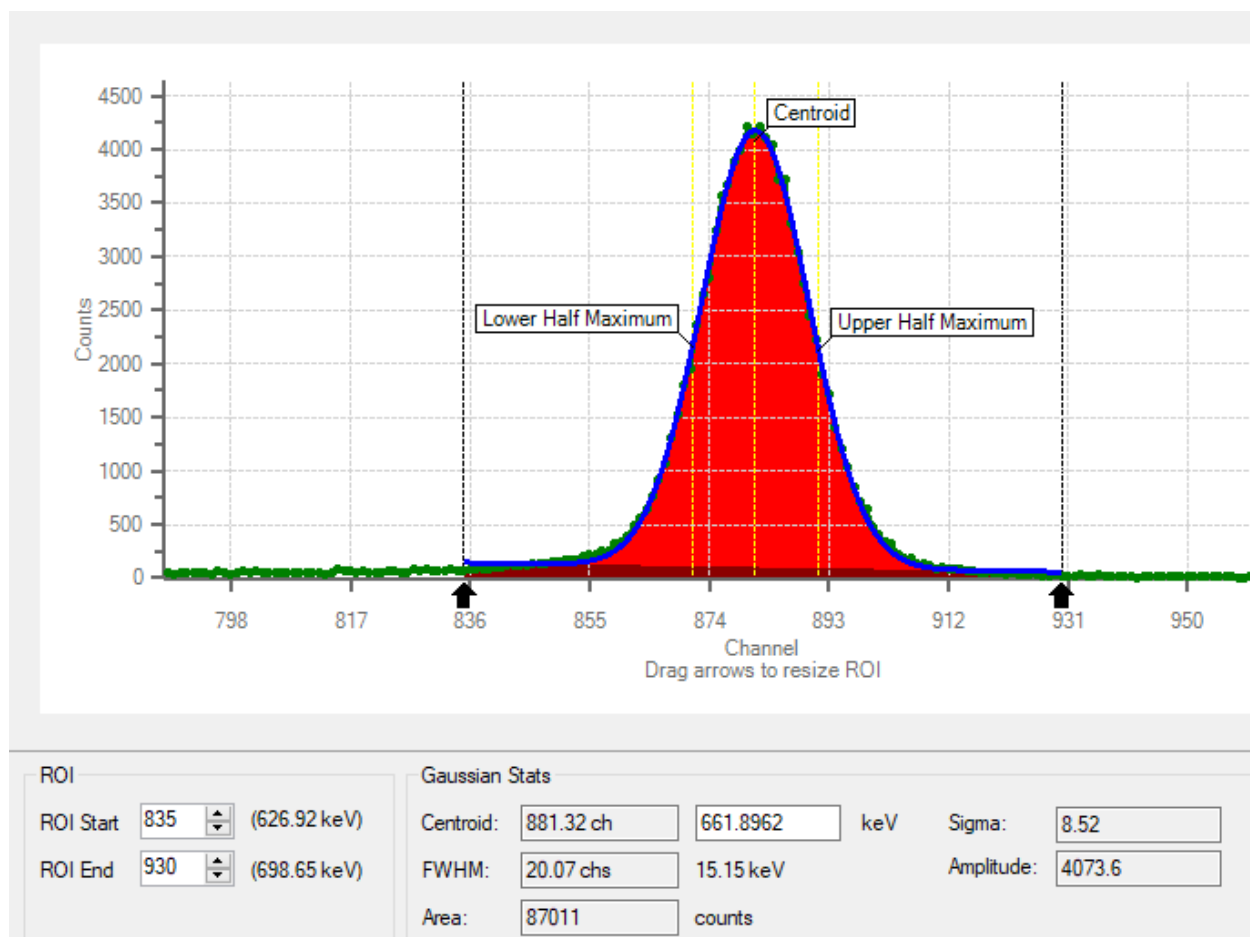Figure 15: Gamma-ray spectrum of sealed 0.898 µCi ^{137}Cs source measured from 0 inches.

Figure 16: Gaussian Stats of data from Figure 15.

In Figure 15, the γ-ray peak is highlighted in red as the region of interest, or ROI. All the data to the left of the ROI is background radiation from the environment. The ROI tool in KSpect is used by hand-picking the "start" and "end" points and generating a gaussian distribution, as seen in figure 16. Figure 16 displays important data such as the centroid, which is compared to 662 keV, the energy of characteristic [137]Cs γ-rays, the FWHM (full-width half maximum) which defines the resolution (accuracy) of the detector, the area of the distribution, and the amplitude,

which is the number of counts (γ-rays) read by the CZT detector. In this case, with the distance between the detector and source being 0 inches, a high count of 4073 was detected at or close to the centroid, and a smooth gaussian curve was created as a result. The centroid was in channel 881.32, which due to calibration is an energy of 661.8962 keV, giving a percent error of 0.016% compared to real value of 662 keV, indicating accurate measurements. The FWHM was given as 20.07 channels (chs), or 15.15 keV. Given the centroid at ch 881.32, this is a FWHM resolution of 2.23%. While this detector claims a resolution of <2%, there could be error stemming from the hand-placing of the start and end of the ROI.
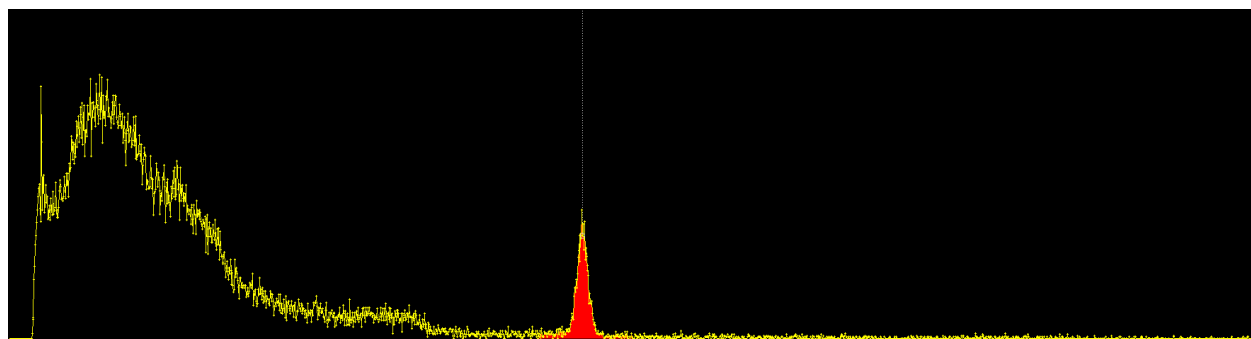

Figure 17: Gamma-ray spectrum of sealed 0.898 μCi ^{137}Cs source measured from 6 inches.
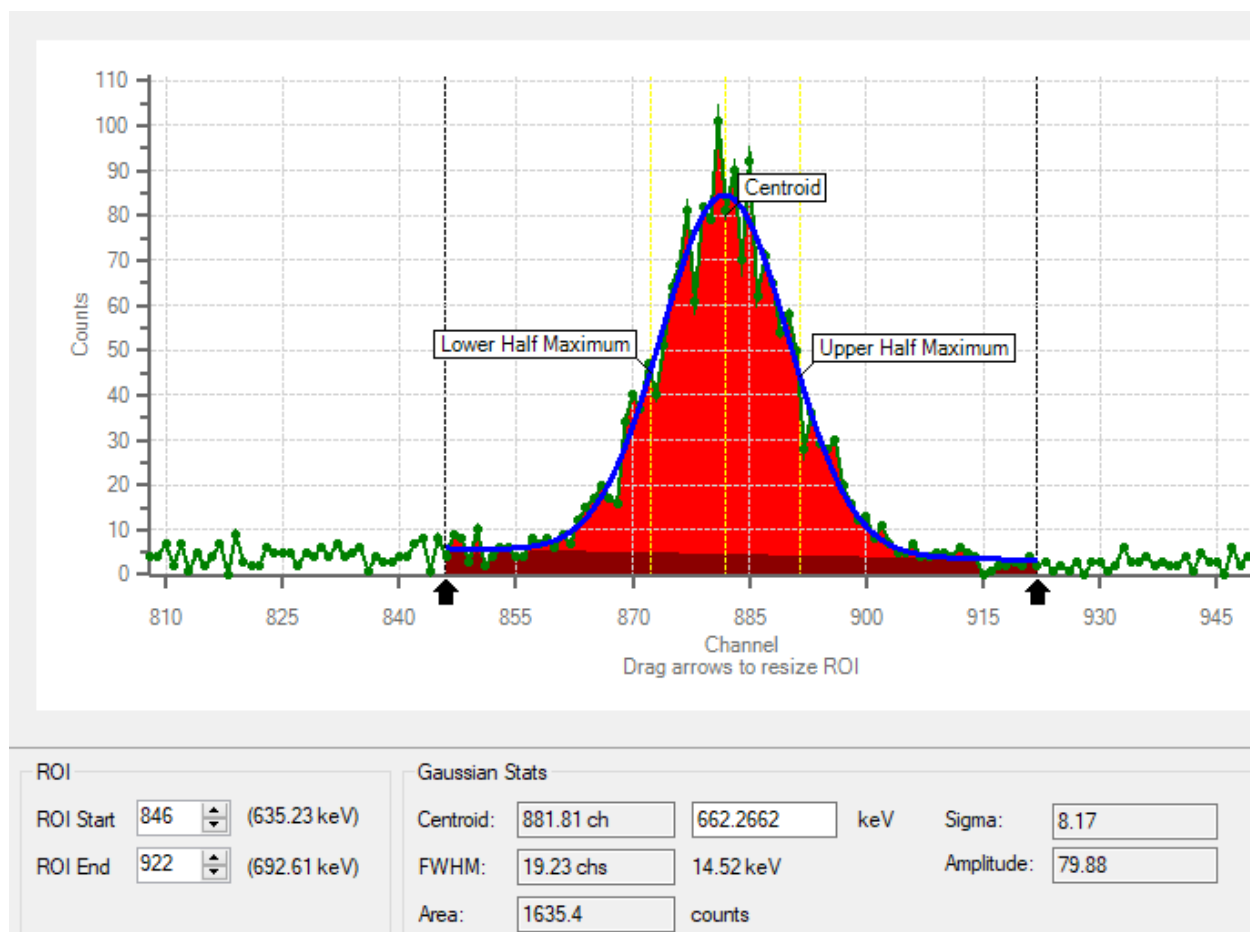
Figure 18: Gaussian Stats of data from Figure 17.

Figures 17 and 18 show data captured from 6 inches away from the source. Immediately a difference in the spectra can be seen comparing Figure 17 to Figure 15, especially comparing the size of the ROI peak compared to the background radiation. Moving the detector 6 inches away from the source causes much less γ-rays to be absorbed due to the inverse square law behavior of radiation emitted isotropically from the source. The stats given in figure 18 give a centroid percent error of 0.04% and a FWHM resolution of 2.18%. In addition, the major difference is the area of the gaussian distribution. The measurement from 0 inches had an area of 87011 counts, whereas

from 6 inches only 1635.4 counts were measured. This indicates an attenuation of 98.12%. This amount of attenuation is very high for such a small distance, but also makes sense because of the small activity of this source.
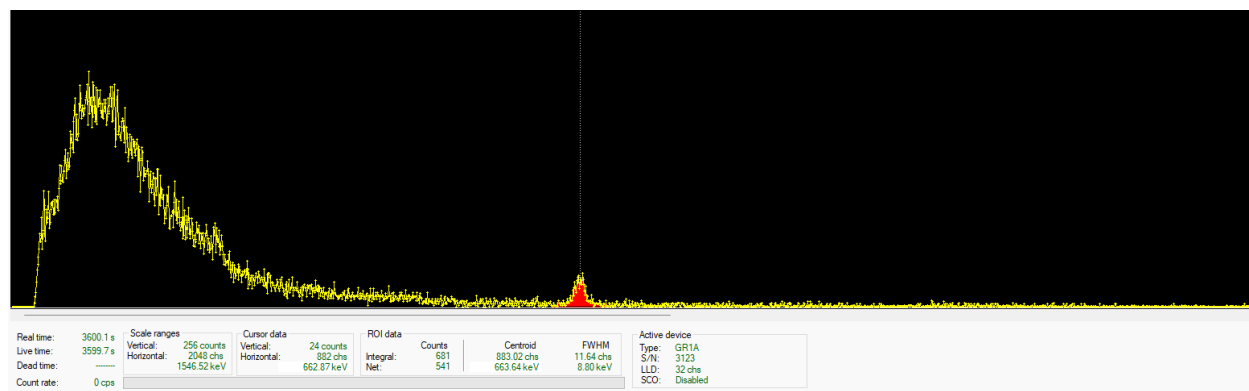

Figure 19: Gamma-ray spectrum of sealed 0.898 µCi ^{137}Cs source measured from 12 inches.
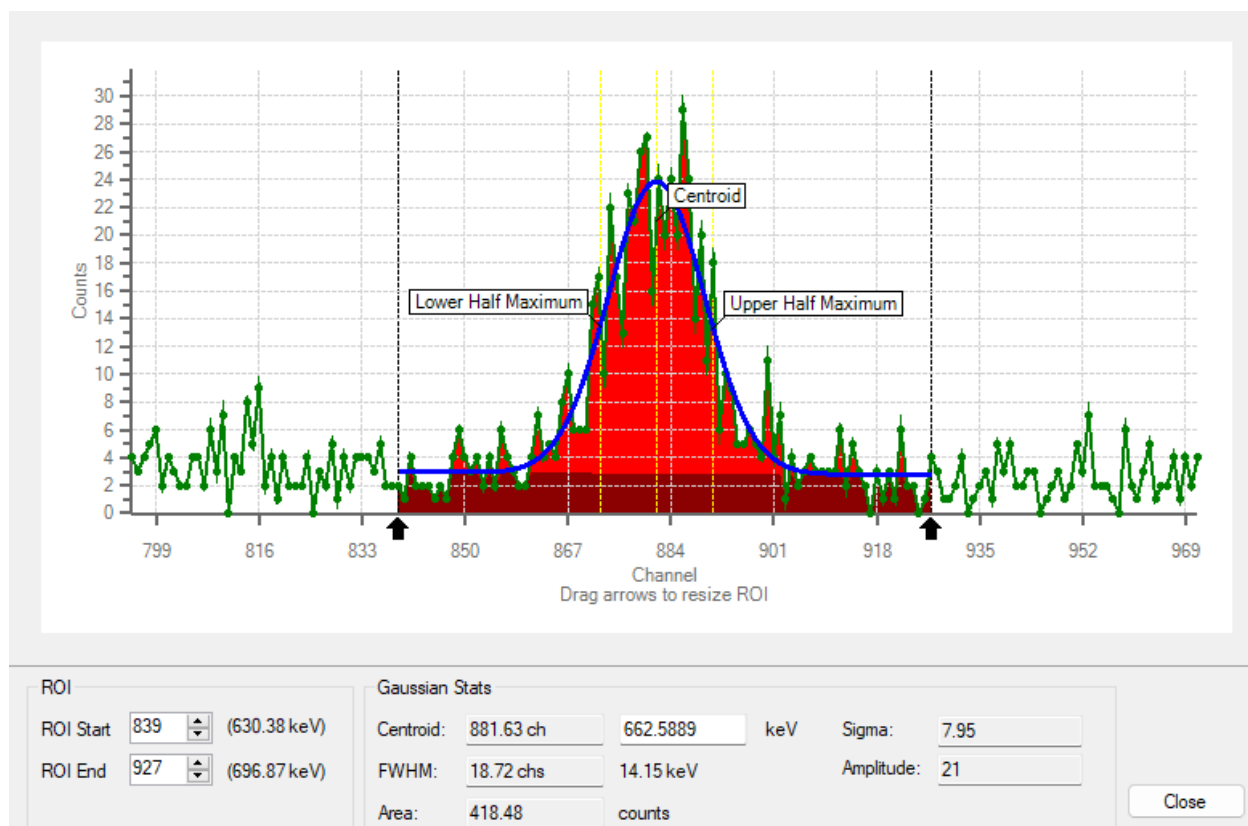
Figure 20: Gaussian stats of data from Figure 19.

Figures 19 and 20 display the data measured 12 inches away from the source. The smaller peak seen in figure 19 signifies how much attenuation there is from this distance. An area of only 418.48 counts gives an attenuation of 99.52%. Comparing to previous spectra from 0 and 6 inches, the peak has dropped in size drastically, which can be seen more clearly when looked at relative to the background radiation. The gaussian for this spectrum yielded a centroid percent error of 0.089% and a FWHM resolution of 2.12%. Figure 20 also shows how imperfect the gaussian curve is becoming due to less data being captured.

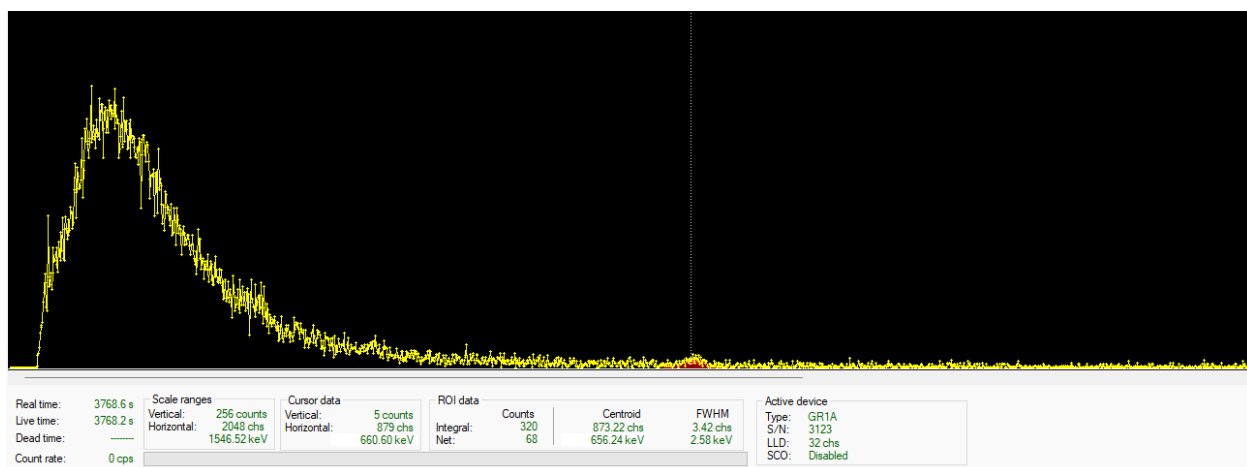Figure 21: Gamma-ray spectrum of sealed 0.898 µCi ^{137}Cs source measured from 24 inches.
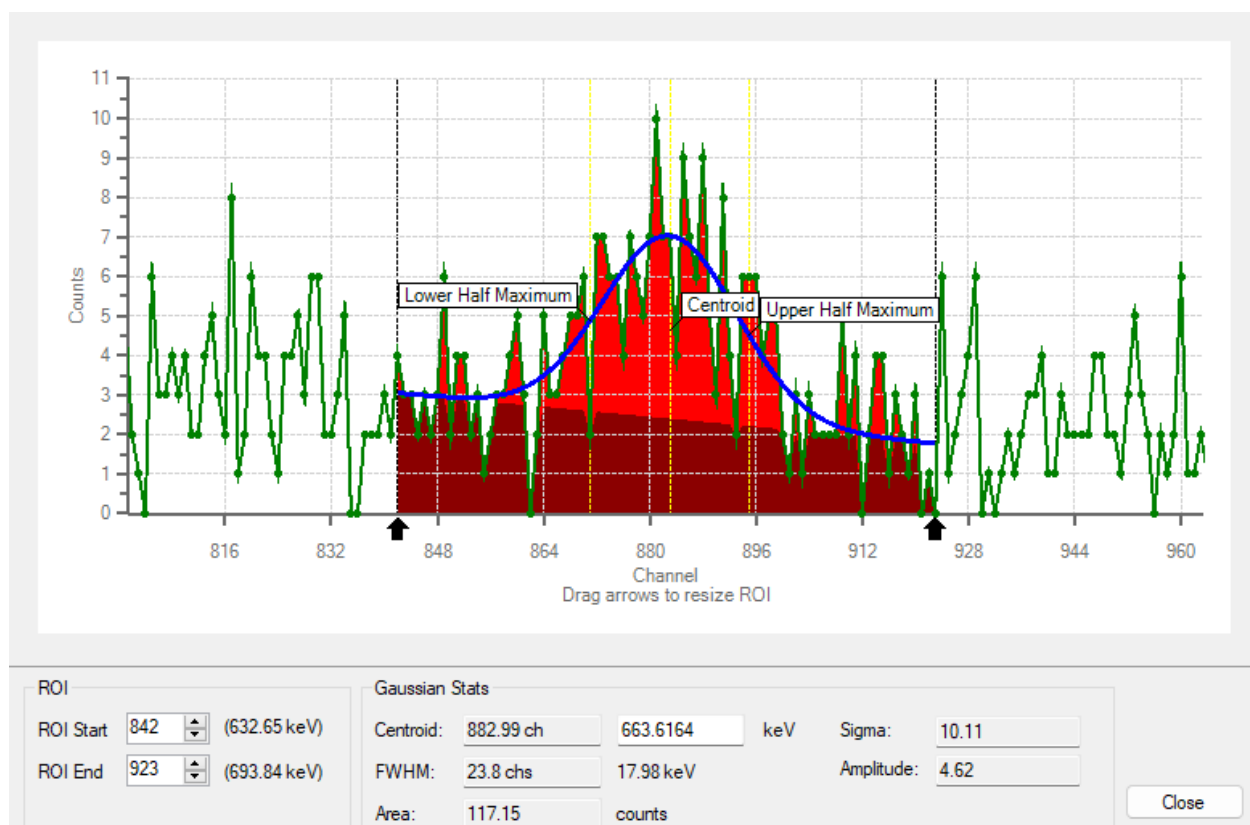

Figure 22: Gaussian stats of data from Figure 21.

Figures 21 and 22 contain the data measured 24 inches away from the source. At this distance, the peak is almost indistinguishable from the rest of the spectrum. As seen in figure 22, the gaussian curve created is messy and barely noticeable. An area of only 117.15 counts gives an attenuation of 99.87%, making the measurement essentially negligent. In addition, the messy data is highlighted in the centroid value, 663.6164 keV, giving a percent error of 0.244%. While this is still a small number, it is three times higher than the error measuring from 12 inches and over twenty times higher than the error measuring from 0 inches, so is a relatively bad result. This is expected, however, and shows how detection ability drastically falls over further distances. The FWHM resolution only worsened a small amount of 2.7%.

In addition to taking measurements from the low activity 0.898 µCi ^{137}Cs source, a higher activity one of 16 µCi was also measured. This was to show how a higher activity would take a longer distance to experience a similar increase in attenuation. The following figures show the spectra and gaussian distributions of measurements from the same distances as the previous measurements, just with the 16 µCi source instead.

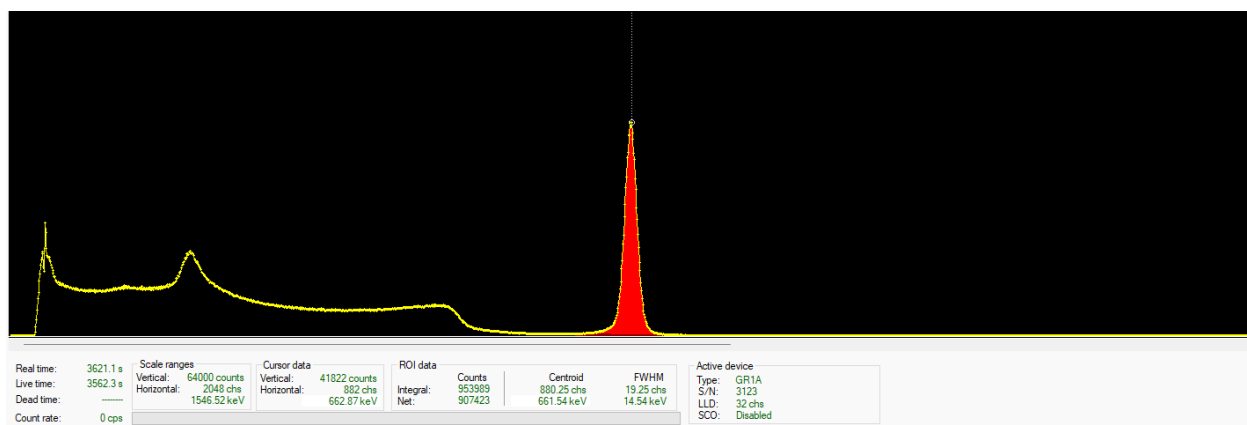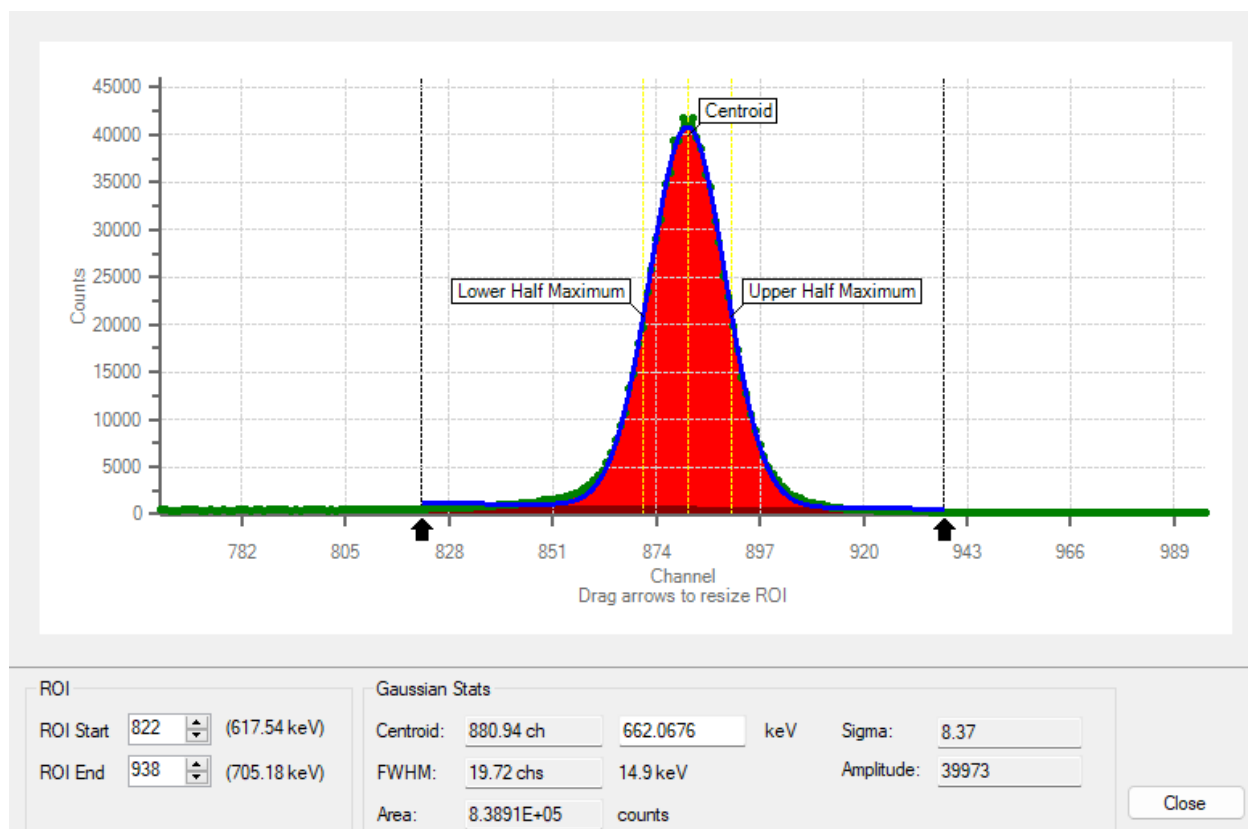Figure 23: Gamma-ray spectrum of sealed 16 µCi ^{137}Cs source measured from 0 inches.

Figure 24: Gaussian stats of data from Figure 23.

Figures 23 and 24 show the data received from measuring the 16 µCi source flush against it. The higher activity can immediately be seen through the eye test when compared to the 0.898 µCi in that the peak seen in Figure 23 is relatively much higher than the background radiation. The stats shown in Figure 24 confirm this, with a very large area count of 8.3891E+05. This amount of data allowed for a very smooth gaussian curve, providing accurate data. This is proven through the centroid value of 662.0676, which has a percent error of 0.01%. The FWHM resolution stayed around the same at 2.24%.

Real time:	3600.4 s	Scale ranges		Cursor data		ROI data				Active device	
Live time:	3597.5 s	Vertical:	2000 counts	Vertical:	555 counts		Counts	Centroid	FWHM	Type:	GR1A
Dead time:	------	Horizontal:	2048 chs	Horizontal:	893 chs	Integral:	32644	881.11 chs	18.68 chs	S/N:	3123
Count rate:	0 cps		1546.52 keV		671.18 keV	Net:	30806	662.20 keV	14.11 keV	LLD:	32 chs
										SCO:	Disabled

Figure 25: Gamma-ray spectrum of sealed 16 µCi ^{137}Cs source measured from 6 inches.
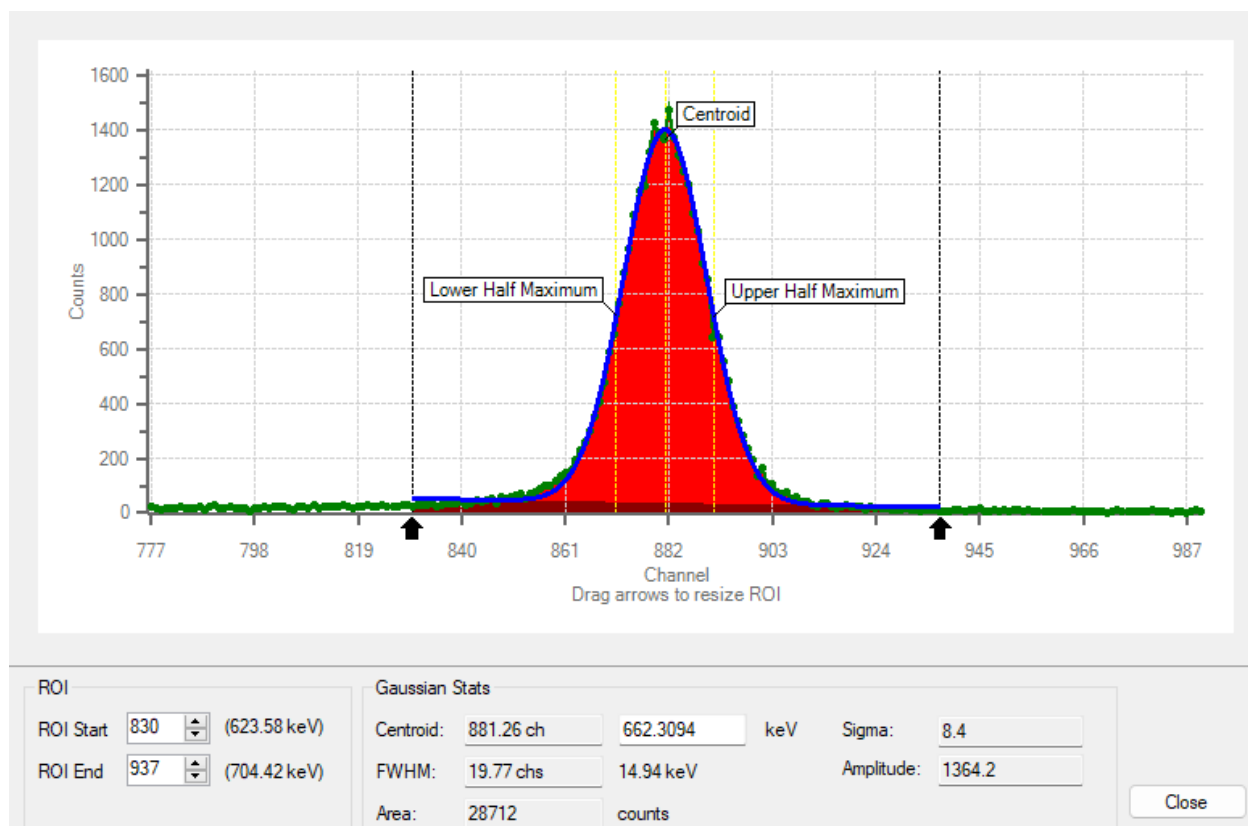
Figure 26: Gaussian stats of data from Figure 25.

Figures 25 and 26 show data captured by measuring the 16 µCi source from 6 inches away. The drastic drop of area seen in figure 26 shows how much distance causes attenuation. An area of 28712 counts gives an attenuation of 96.58%. The higher activity than the previous sealed source used does allow for higher readings from a distance, as seen by the difference in counts at the same distance. At 6 inches with the 0.898 µCi source, an area count of 1635.4 was measured, whereas with the 16 µCi source, an area count of 28712 was measured, an approximately 18 times increase. This amount alignes with the 16 µCi source having an approximately 18 times stronger

activity than the 0.898 µCi source. The centroid percent error for this data set is 0.0467% and the

FWHM resolution is 2.24%, staying consistent across the experiments.

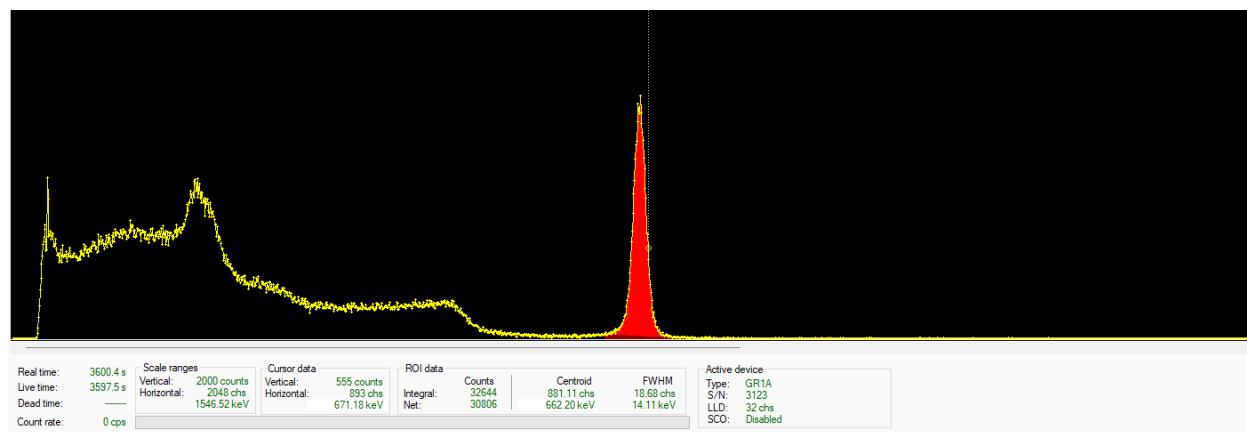

Figure 27: Gamma-ray spectrum of sealed 16 µCi ^{137}Cs source measured from 12 inches.
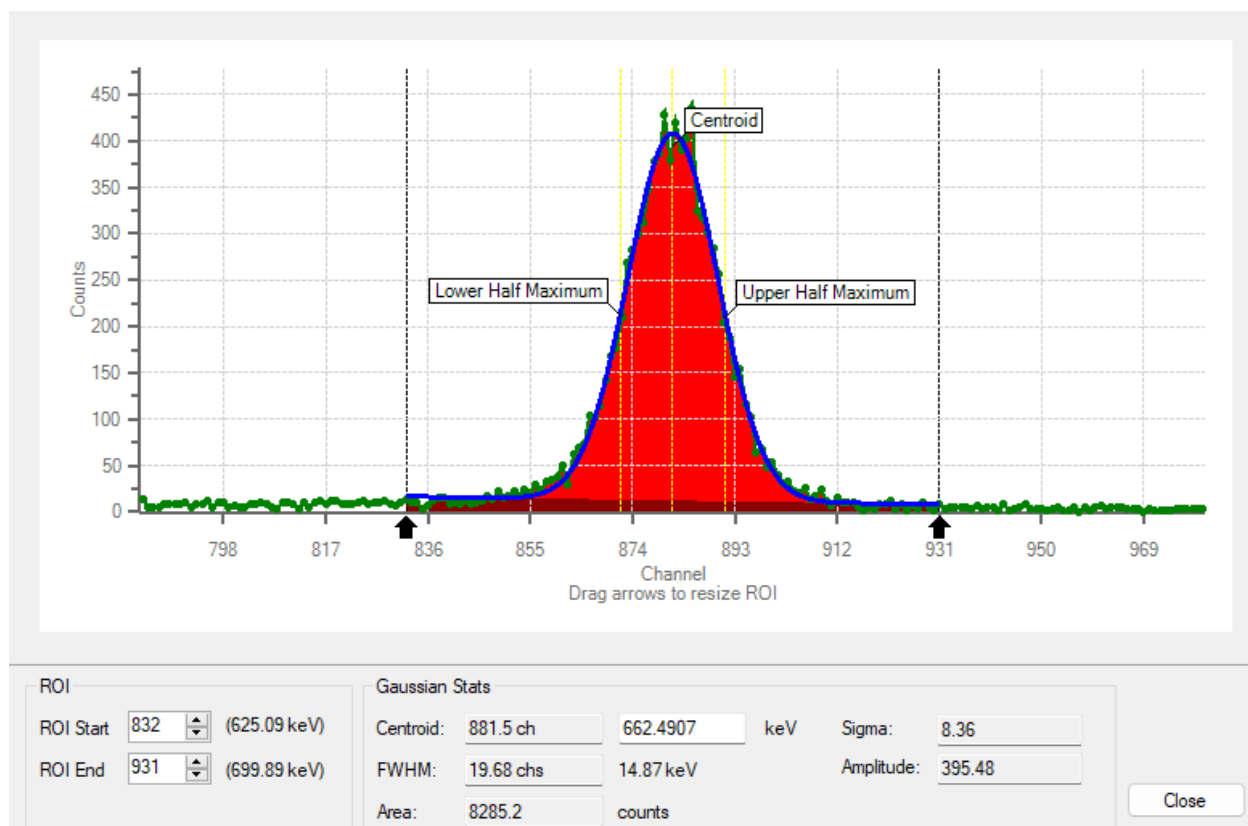
Figure 28: Gaussian stats of data from Figure 27.

Figures 27 and 28 contain data from measurements taken from 12 inches away from the sealed source. In contrast to how messy the gaussian curves started becoming from this distance with the weaker 0.898 µCi source, the stronger 16 µCi course allows for much higher counts, and therefore smoother gaussian curves. This makes for more accurate data. An area of 8285.2 counts gives a distance attenuation of 98.76%. The centroid value is 662.4907 which has a percent error of 0.0741% and the FWHM resolution stays consistent at 2.23%.

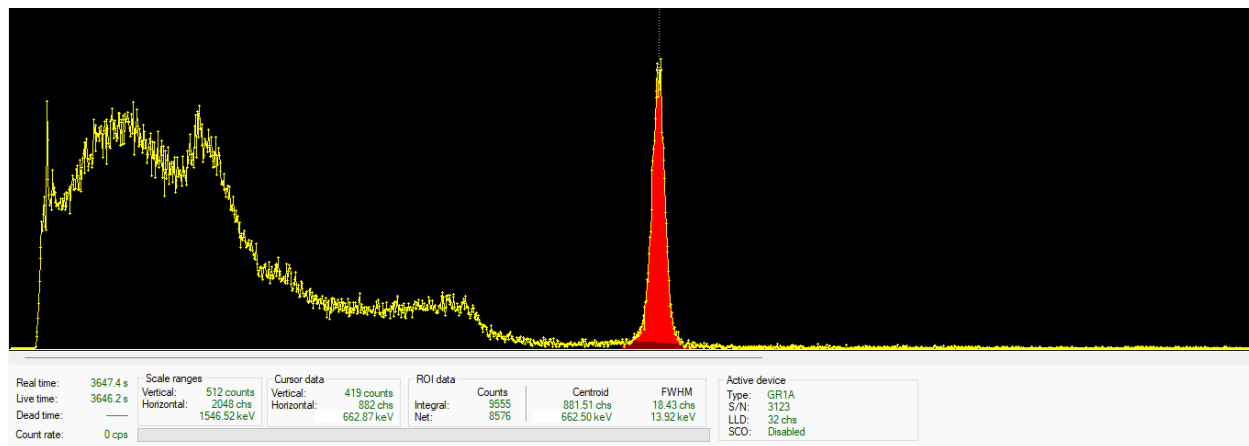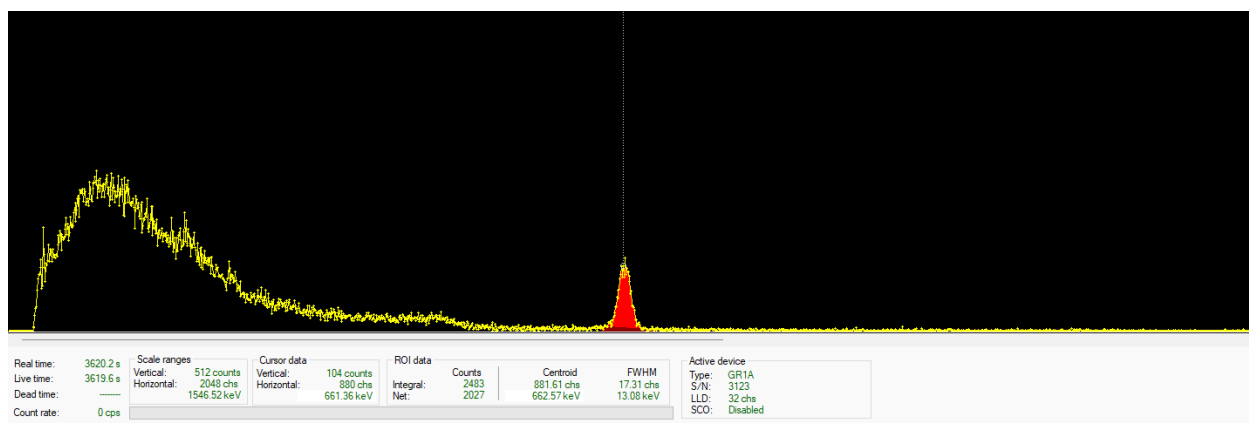Figure 29: Gamma-ray spectrum of sealed 16 μCi ^{137}Cs source measured from 24 inches.
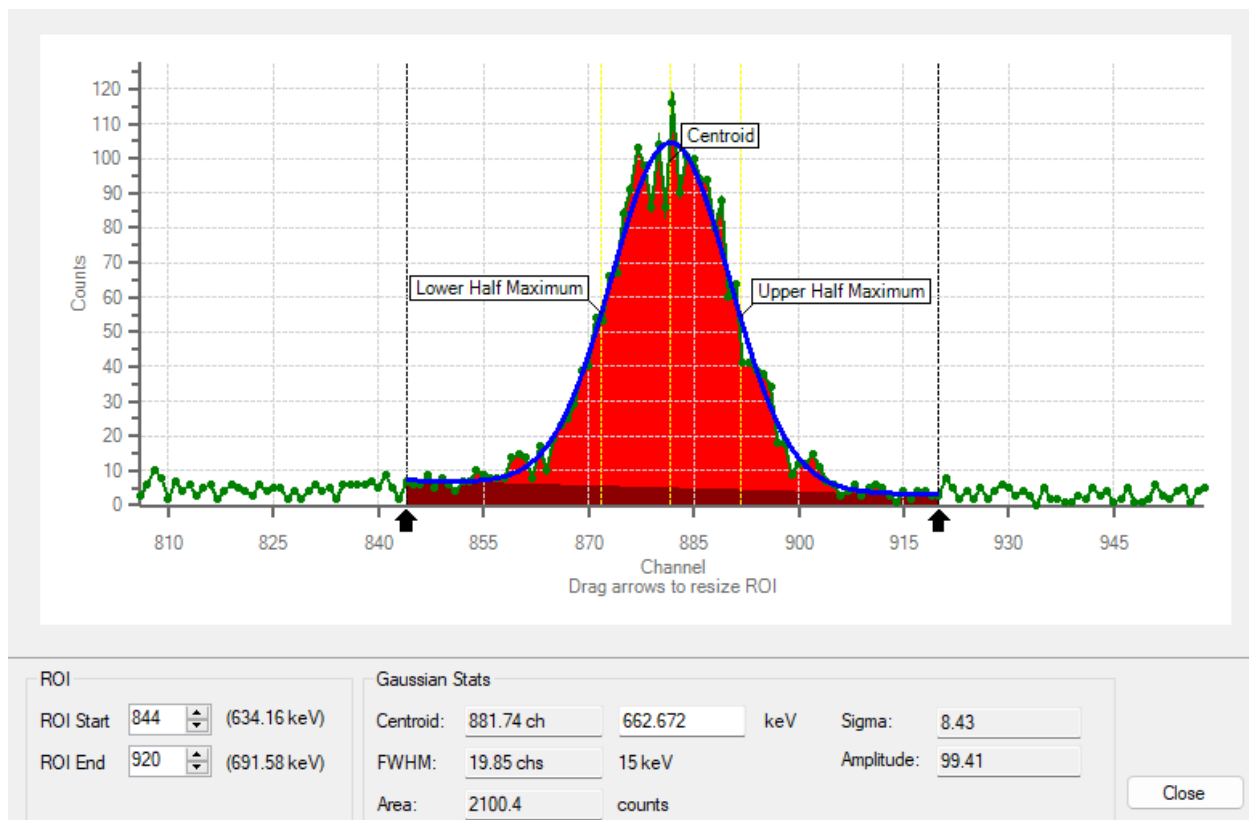
Figure 30: Gaussian stats of data from Figure 29.

Figures 29 and 30 show the spectrum and Gaussian distribution of measurements taken 24 inches from the source. Similar to the 0.898 μCi source, measurements fell in accuracy even more from this distance. However, due to the stronger activity, these measurements are still viable, which can be seen by the gaussian curve still being generally smooth. It is not as smooth compared to the closer measurements, however, which is reflected in the numbers. The centroid percent error is 0.102% and the FWHM resolution stays stagnant at 2.25%. The attenuation from this distance is 99.75%. This is a very high attenuation, but the long exposure of the source mitigates this and still allows for a decent spectrum to be generated.

		Scale ranges		Cursor data		ROI data					Active device	
Real time:	3600.1 s	Vertical:	256 counts	Vertical:	18 counts			Counts	Centroid	FWHM	Type:	GR1A
Live time:	3599.7 s	Horizontal:	2048 chs	Horizontal:	885 chs	Integral:	654		879.18 chs	13.38 chs	S/N:	3123
Dead time:	0.0 %		1546.52 keV		665.13 keV	Net:	493		660.74 keV	10.11 keV	LLD:	32 chs
Count rate:	0 cps										SCO:	Disabled
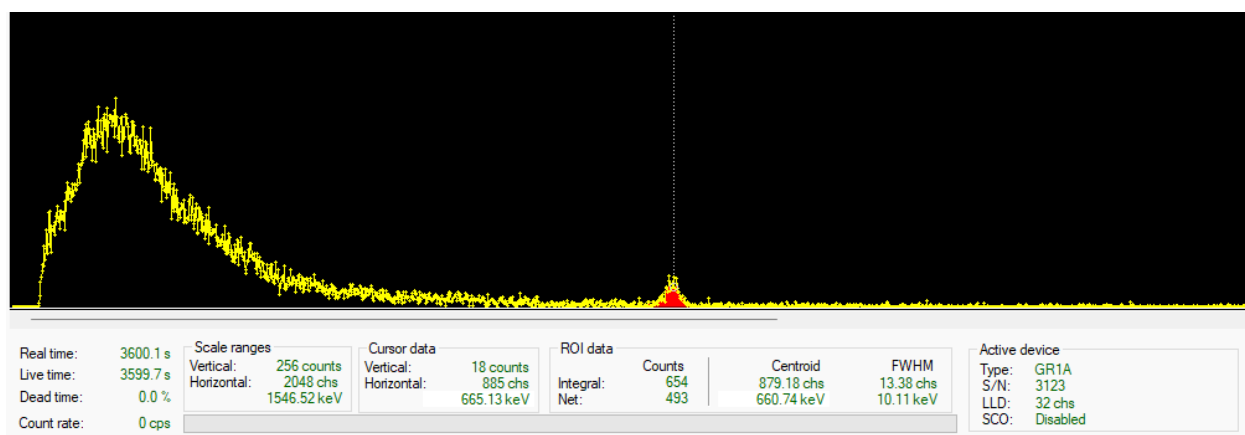
Figure 31: Gamma-ray spectrum of sealed 16 μCi ^{137}Cs source measured from 48 inches.
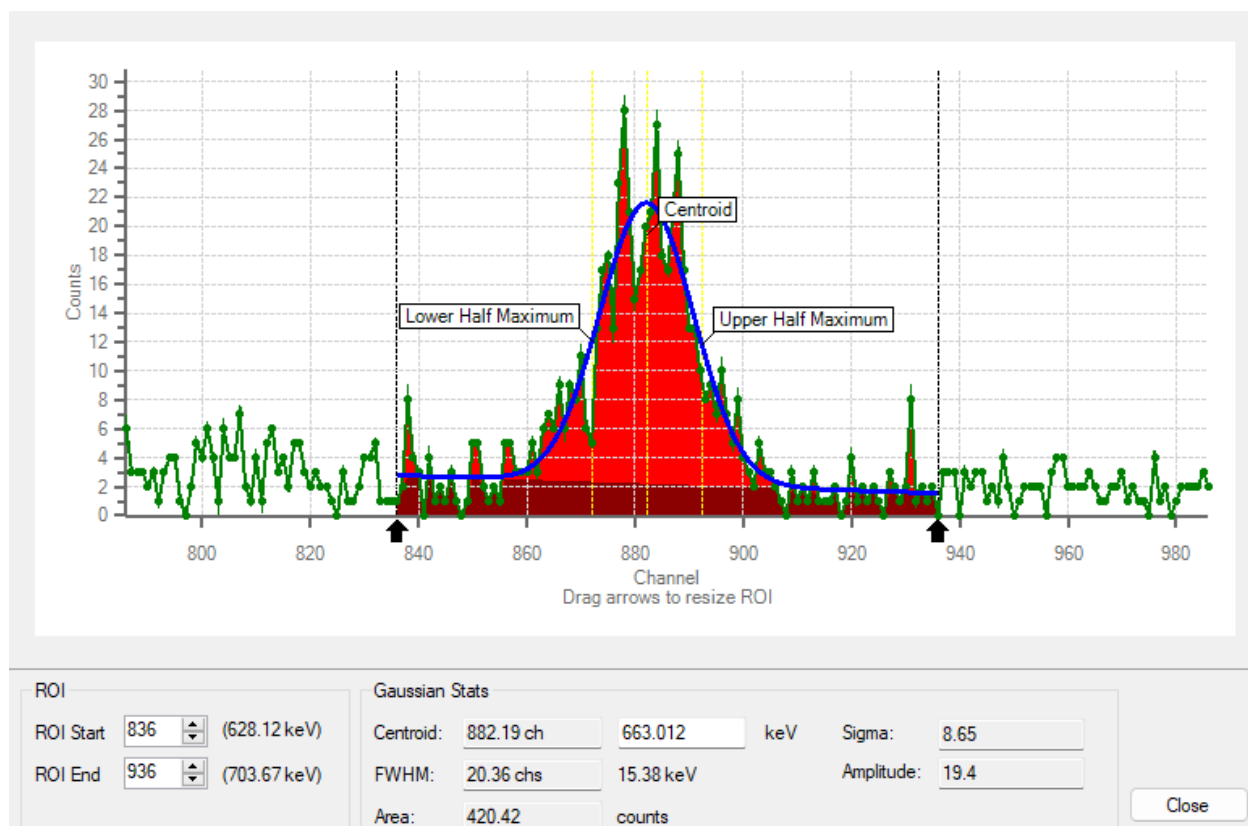
Figure 32: Gaussian stats of data from Figure 31.

To explore the distance limits of measuring the 16 µCi source, it was also measured from 48 inches away, as shown in the data in figures 31 and 32. Even from this distance, the detector was still able to pick up the source with a centroid percent error of 0.153%. While this is high compared to previous measurements, it is still much lower than the error from measuring the 0.898 µCi source from 24 inches. The count area plummeted down to 420.42, representing a 99.95% attenuation.

In addition to examining attenuation purely through distance, attenuation through an absorptive material was also experimented with. A method to deal with leaks from tanks would be

to fix wattles filled with absorptive materials to the exterior of the tank to absorb the leaking materials [68-70]. If this were the case, the dense material would also attenuate the gamma rays, leaving less of a signature for a detector to detect. To test this, a prototype wattle 3 inches thick filled with Zeolite was placed in-between the 0.898 µCi source and CZT detector. Measurements were taken from flush against the wattle (3 inches from the source), 3 inches from the wattle, and 9 inches from the wattle (6 inches and 12 inches from the source respectively). The following figures show the gaussian distributions of each distance.
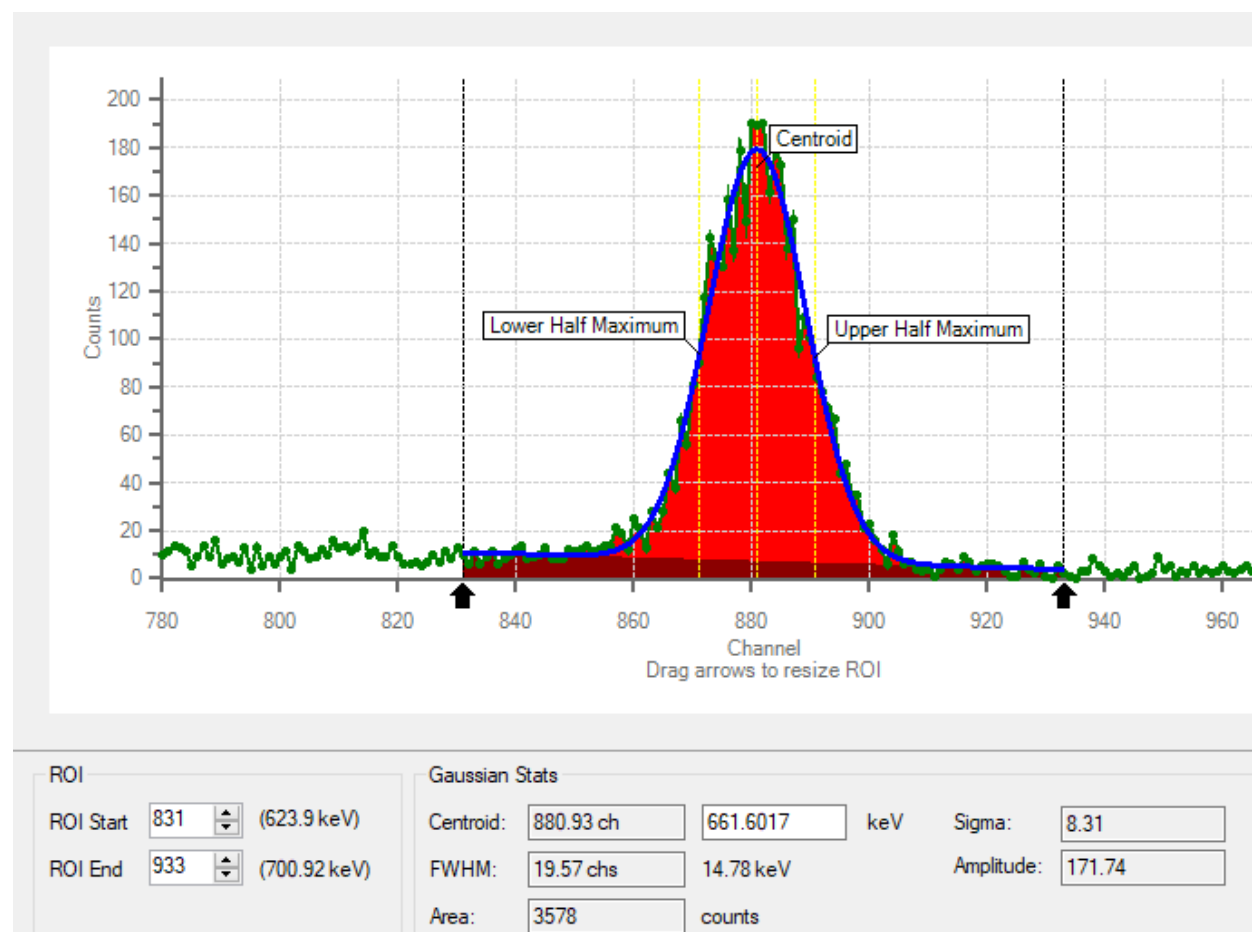
Figure 33: Gaussian stats of data from measurements with Zeolite attenuation from 3 inches.
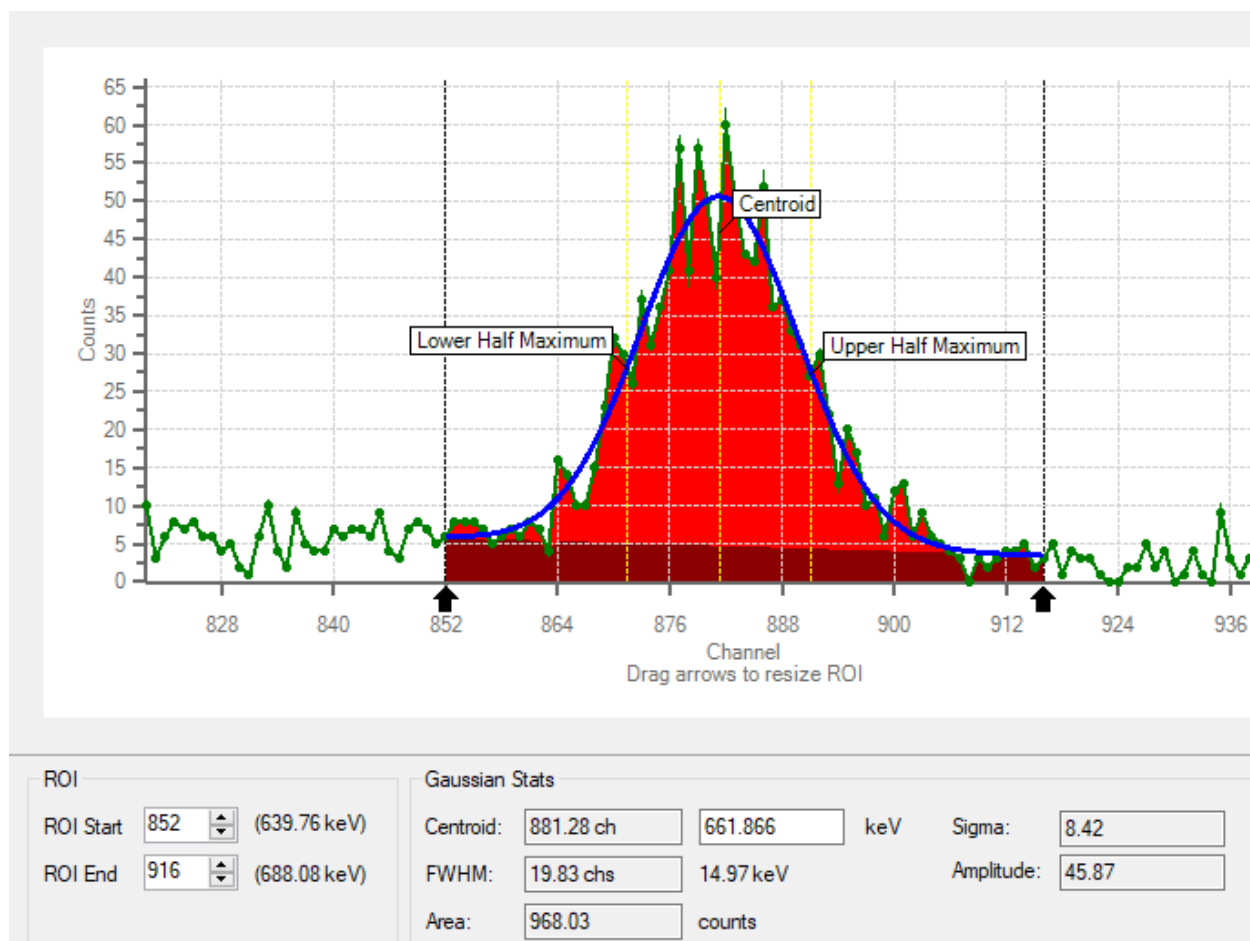
Figure 34: Gaussian stats of data from measurements with Zeolite attenuation from 6 inches.

Figure 35: Gaussian stats of data from measurements with Zeolite attenuation from 12 inches.

Examining the gaussian stats, it is seen that the Zeolite vastly increases the attenuation of the emitted gamma rays. Similar stats to compare are the count areas from 6 and 12 inches away from the source. With only air between the source and detector, the count areas from 6 and 12 inches are 1635.4 and 418.48 respectively. With the Zeolite in between, these count areas are 968.03 and 251.15 respectively. This is a 41% and 40% drop respectively, not only showing how much the Zeolite attenuates, but also showing the consistency in measurements.

49

4.2 Thermal Imaging

The FLIR Duo-R thermal camera was used to image and video different heated metal objects, such as a small rod, a ring, a longer rod, and a plate. Each object was heated by heating tape to a temperature sufficiently higher than the surroundings, and while it was imaged, a thermocouple was used simultaneously to verify the temperature being shown by the camera was accurate within its range. Table 2 contains the IR camera and thermocouple comparisons. The table used as the background in the imaging was measured as 26 degrees Celsius by the thermal camera and 25.3 degrees Celsius by the thermocouple. The camera measurement could be skewed by the reflections in the table.
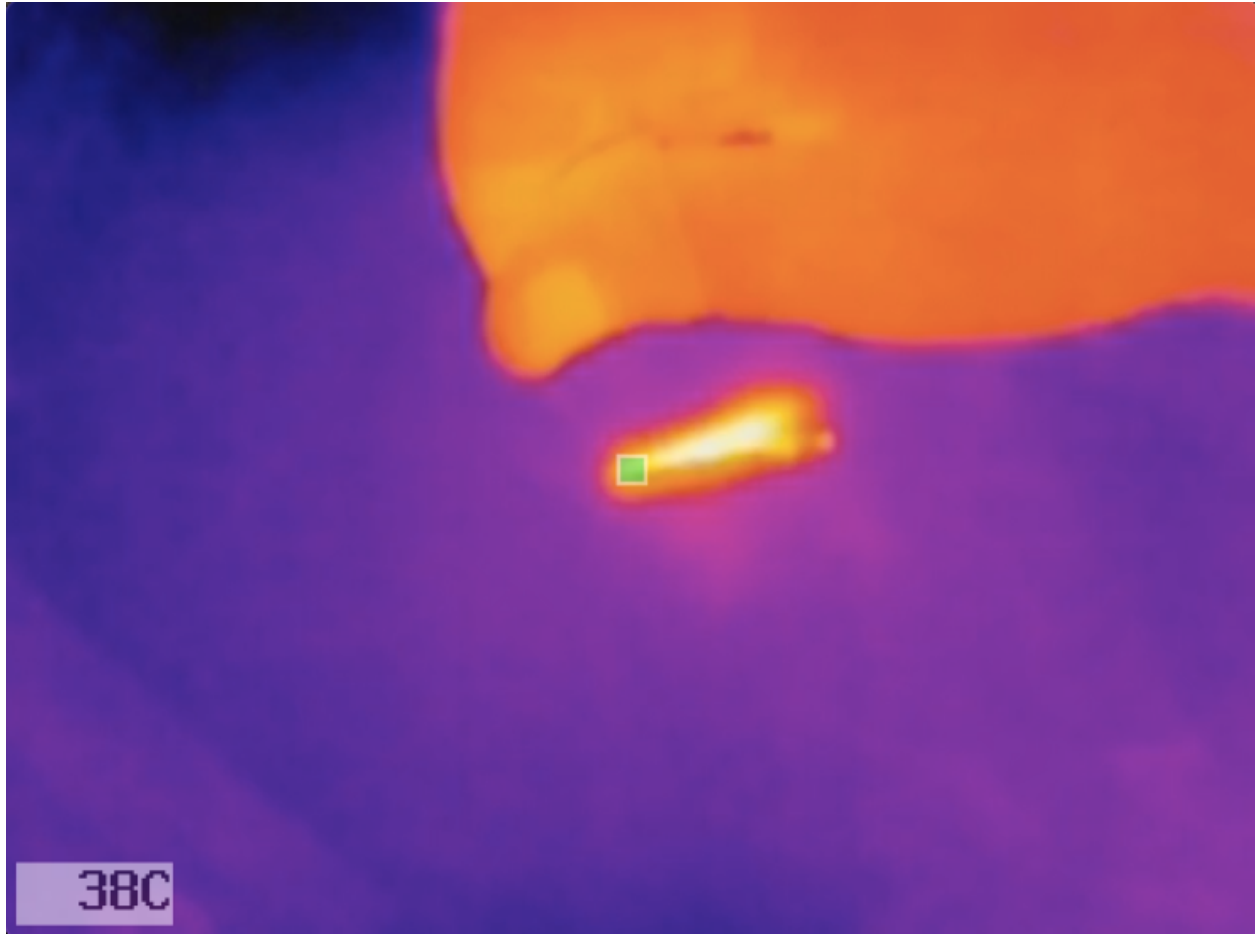
Figure 36: Thermal camera image of the heated small rod.

The long rod imaged was a metal ruler. It was heated and measured two separate times to test different temperatures. Because of the nature of the heating tape, it would not be flush against the face of the ruler. Therefore, the thin edges of the ruler were the hotter areas, with the faces being heated more from conduction from the edges. This adds some error to the measurements.
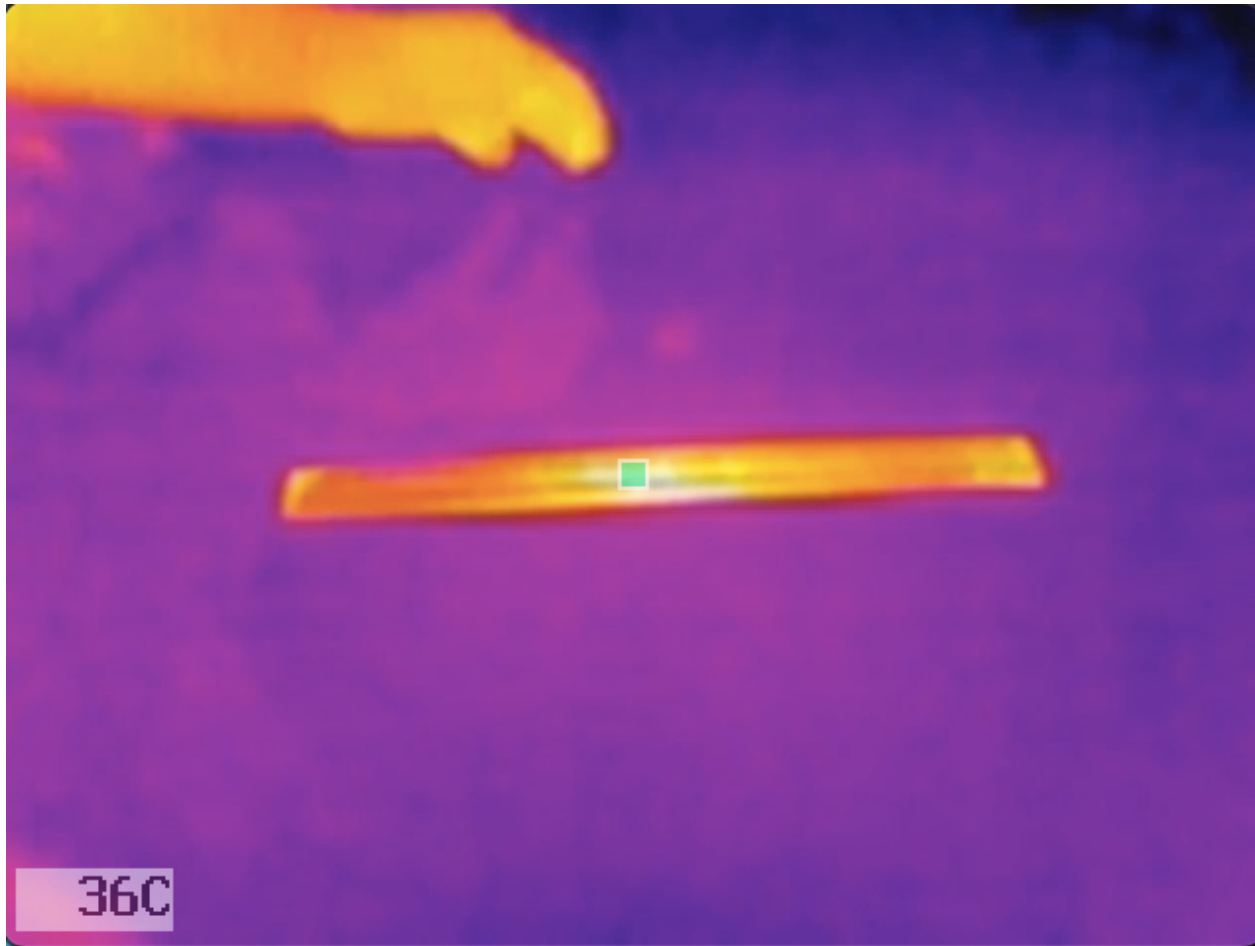
Figure 37: Thermal camera image of a heated metal ruler.
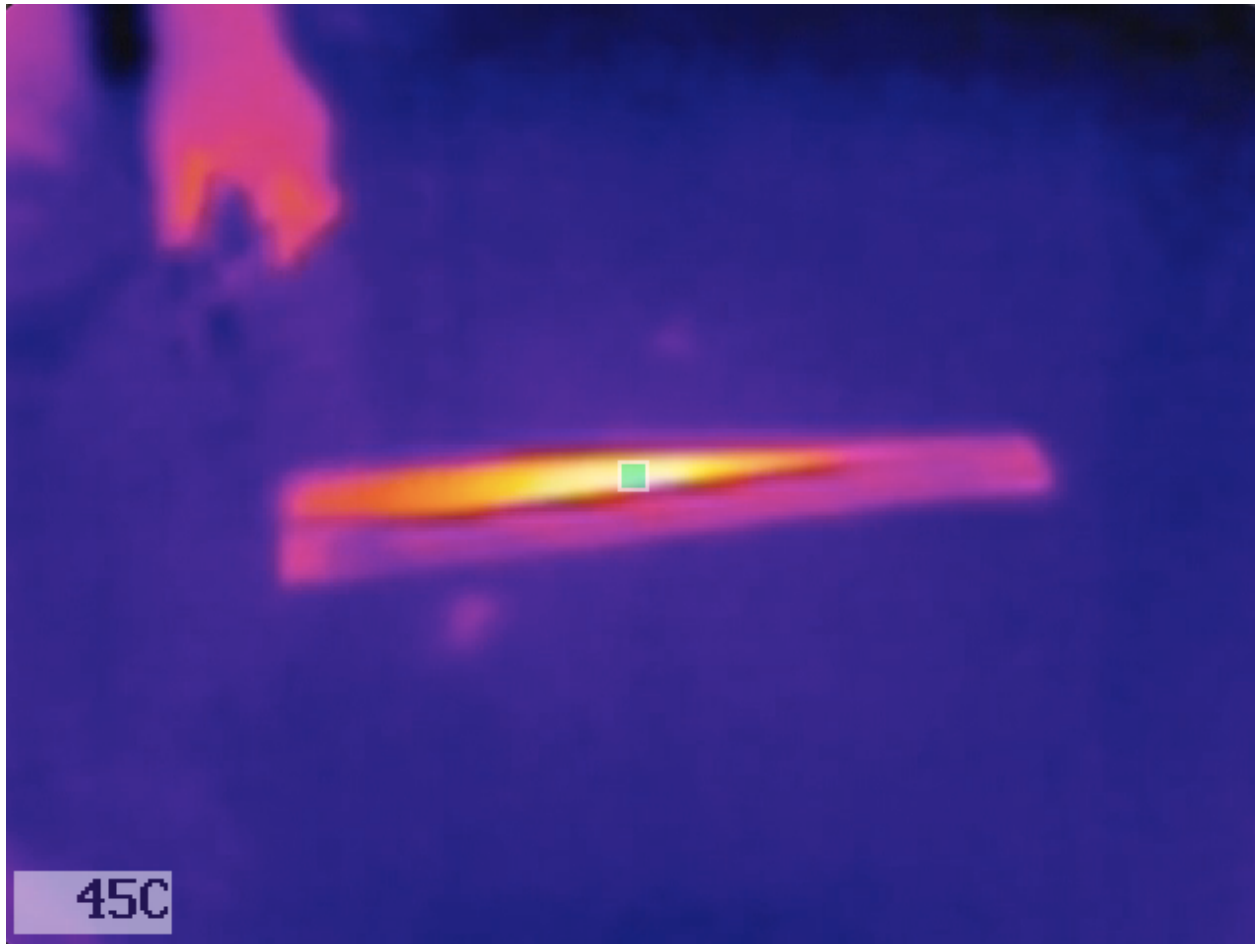
Figure 38: Thermal camera image of heated metal ruler.

Figures 37 and 38 show two different temperatures measured of the same object, a metal ruler. The stark color contrast between "hot" and "cold" is obvious, but there is also the different in "cold" between the two pictures. In figure 38 where the ruler is 9 degrees higher, the surroundings are a darker blue to indicate the stronger difference in temperature.
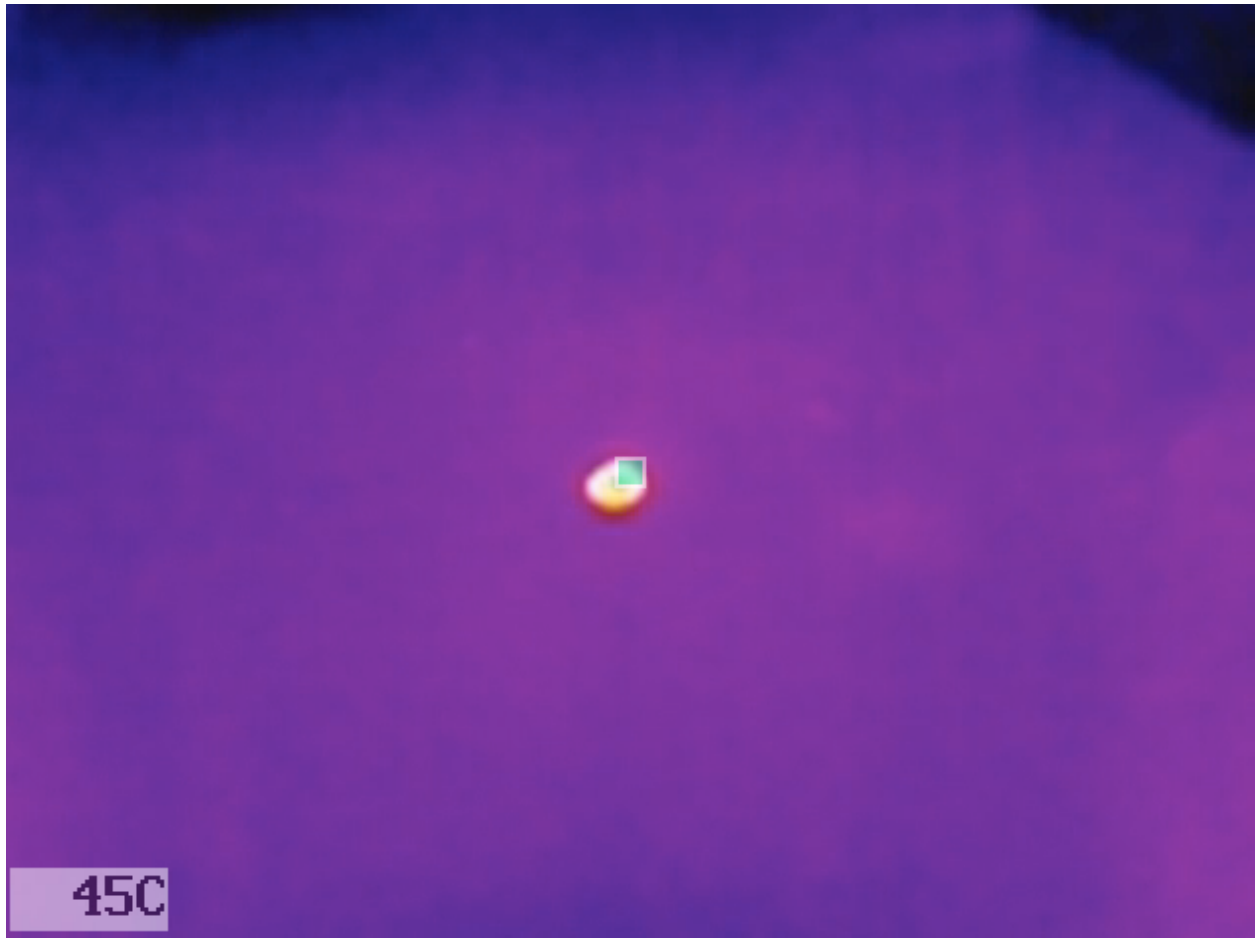
Figure 39: Thermal camera image of heated metal ring.
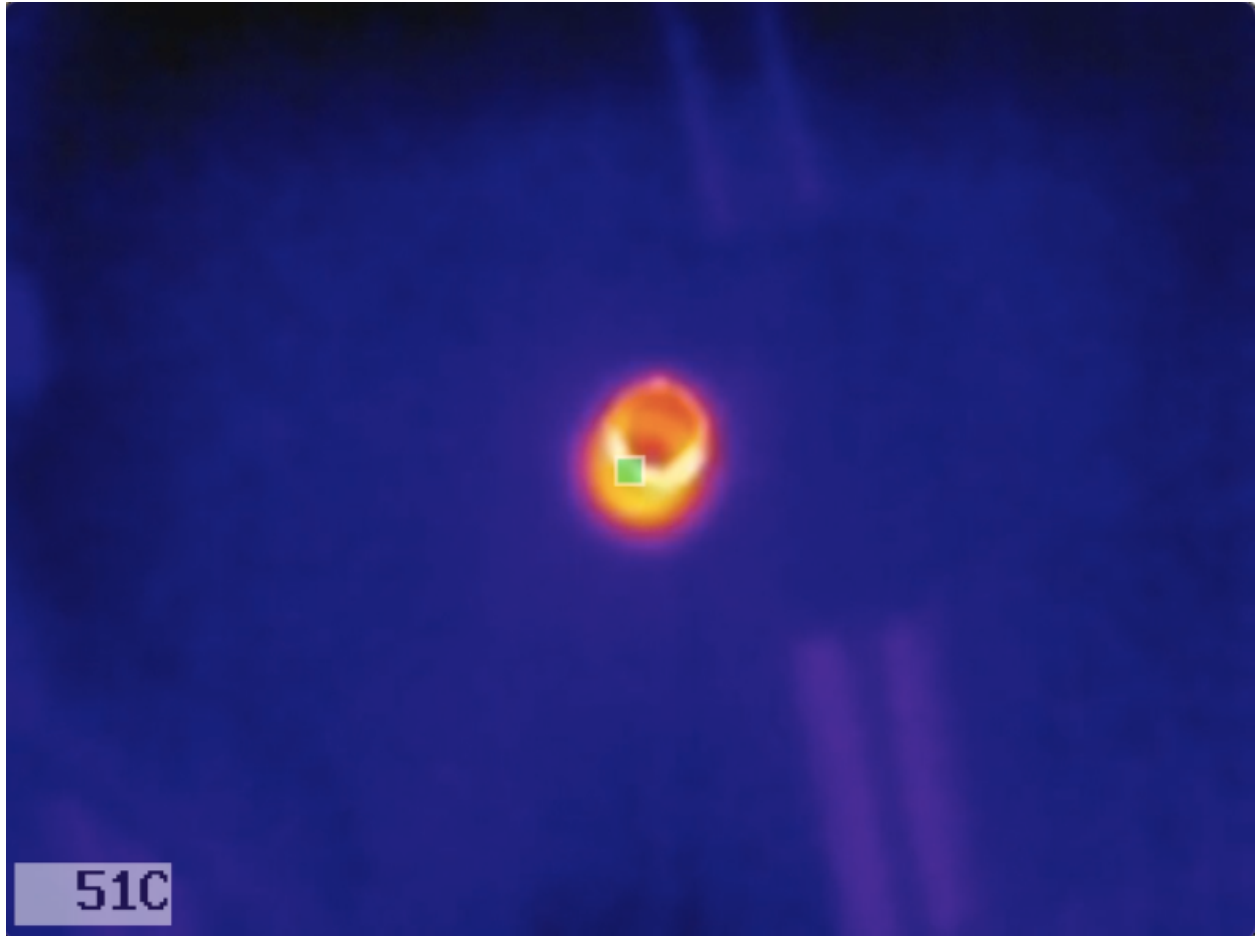
Figure 40: Thermal camera image of heated metal ring.

Similar to the metal ruler, the metal ring images show the same darker blue surroundings in the higher temperature image. The camera was also in a different position for figure 40 than figure 39, thus the size discrepancy between the two images.
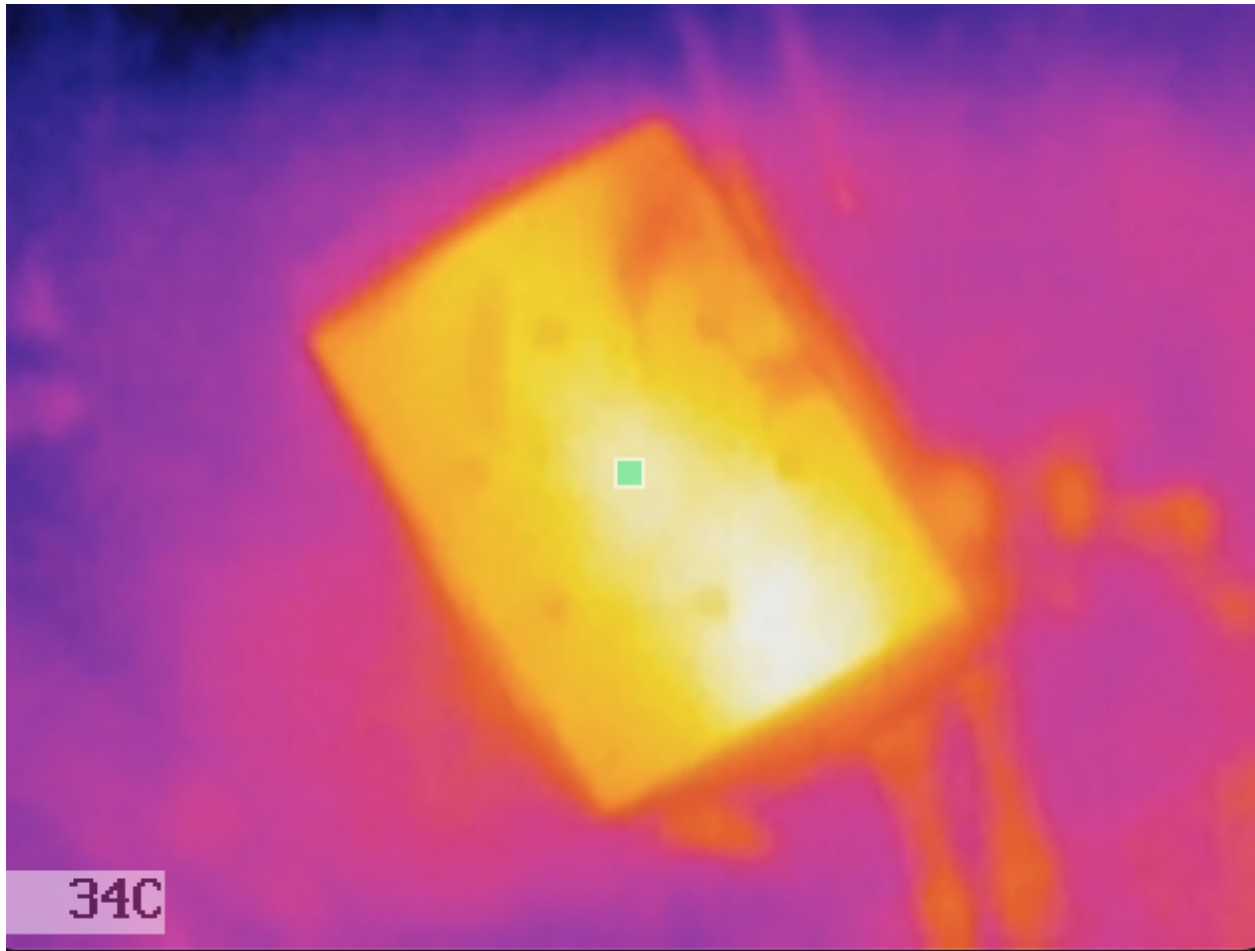
Figure 41: Thermal camera image of heated metal plate.
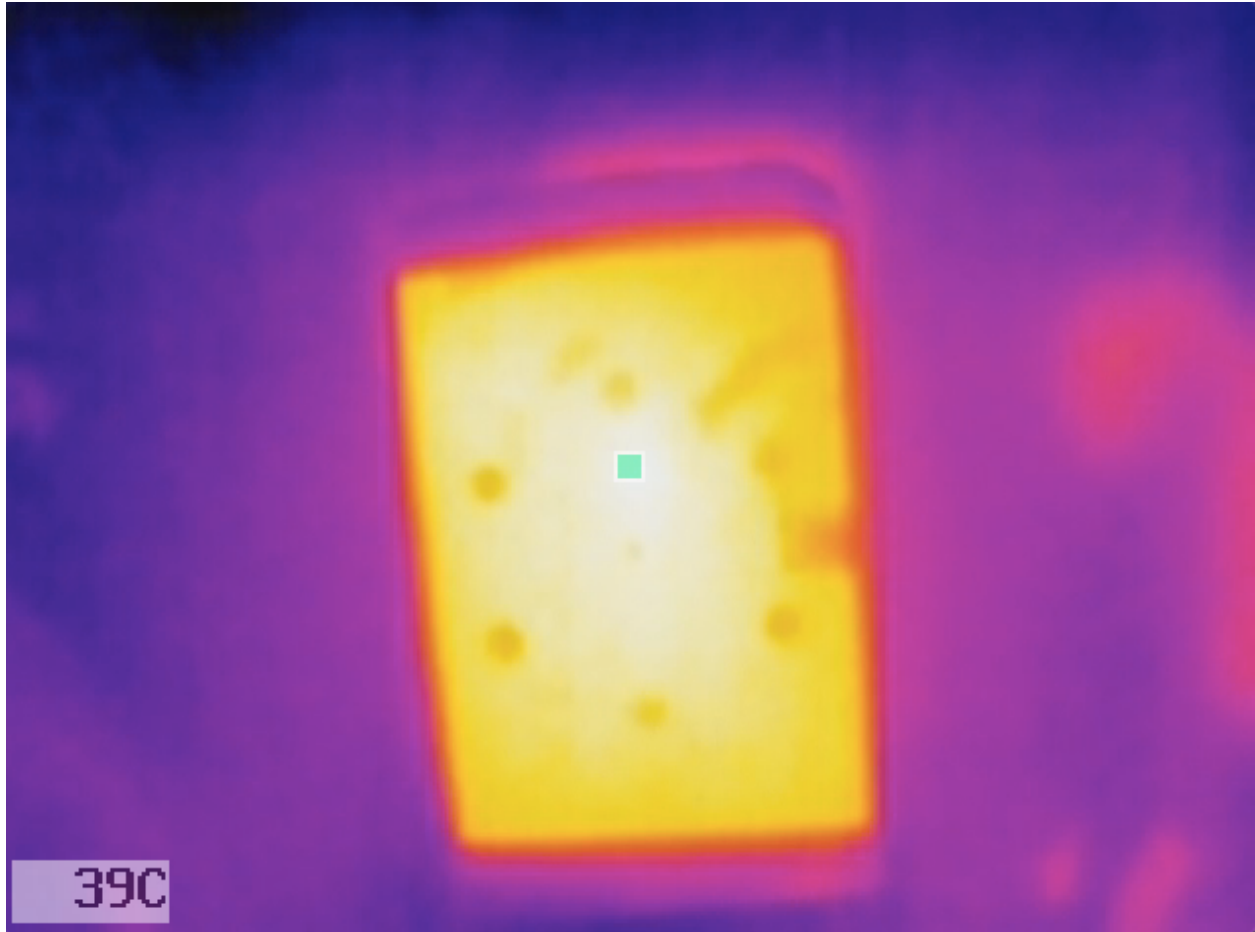
Figure 42: Thermal camera image of heated metal plate.

The metal plate provided a challenge in getting an accurate reading because of its reflective property. To overcome this, a piece of black tape was placed over it during heating and imaging. In addition to eliminating the reflection, the tape also allowed for the imaging of heat through a medium. Not only is the plate visible, but its characteristics of drilled holes are also visible despite the tape being on top. This is an important factor in thermal imaging being useful for seeing through different media.

Metal Object (Figure #)	IR Camera Reading (degrees Celsius)	Thermocouple reading (degrees Celsius)	% Difference
Rod (36)	38	38.4	1.05%
Ruler (37)	36	39.5	9.27%
Ruler (38)	45	48.7	7.898%
Ring (39)	45	50	10.53%
Ring (40)	51	55.6	8.63%
Plate (41)	34	32.7	3.898%
Plate (42)	39	40.6	4.02%

Table 2: Results of thermal camera imaging of different metal objects.

Looking at figures 36 through 42, even an object heated to just 10 degrees above the ambient surroundings is strikingly viewable. As the temperature of the object increased, the color contrast also increased. As mentioned, the surroundings changed to a darker blue to indicate the stronger difference in temperature to the heated object. Imaging different shapes and sizes of objects shows how the camera can detect anything. Figure 40 shows the camera can differentiate the ring from being a disk, as indicated by the blue interior of the ring. Analyzing the data in table 2 leads to interesting conclusions. The differences between temperatures measured with the camera and thermocouple were not very consistent. The temperature measured by the thermocouple tended to be higher than that measured by the camera. This difference doesn't indicate failure, however, as the error associated with the camera temperature measurement is +/- 5^{oC} as mentioned before.

The challenges associated with these experiments were the non-precise heating, reflection, and quick cooling of the objects. The heating tape could be set to a high temperature, but the nature of its thick geometry didn't allow for close contact to all points of the small objects. Thus, when it came to measuring the temperature of the object, it was difficult to gather readings at the same location. The spot the camera was recording may not have been the exact spot the thermocouple was measuring by hand. This may have contributed to some error in measurements. The transfer from heating tape to measuring location allowed time for the objects to cool through the air, making the time frame to measure smaller and could have led to inaccuracies as well. Finally, the reflections in objects provided a difficult challenge. The table where measurements took place had some reflective properties and thus the lights from above were visible in the camera. This was not much of a problem in measuring the objects, however, because they were a higher temperature and thus highlighted in the images. The metal plate, however, was not. The metal plate not only reflected the lights from above, but the camera itself looking down from above. This is initially why the black tape was placed on it, to reduce reflection. The application of seeing through a medium was an extra finding during this experimental process.

4.3 Ultrasonic Signatures

The microphone used to complete these experiments is the iSV1611 USB microphone from Roga Instruments. The microphone included a calibrator with settings at 94 dB and 114 dB. The spectra from that calibration, as well as the changes when switching between them, are shown in the following figures.
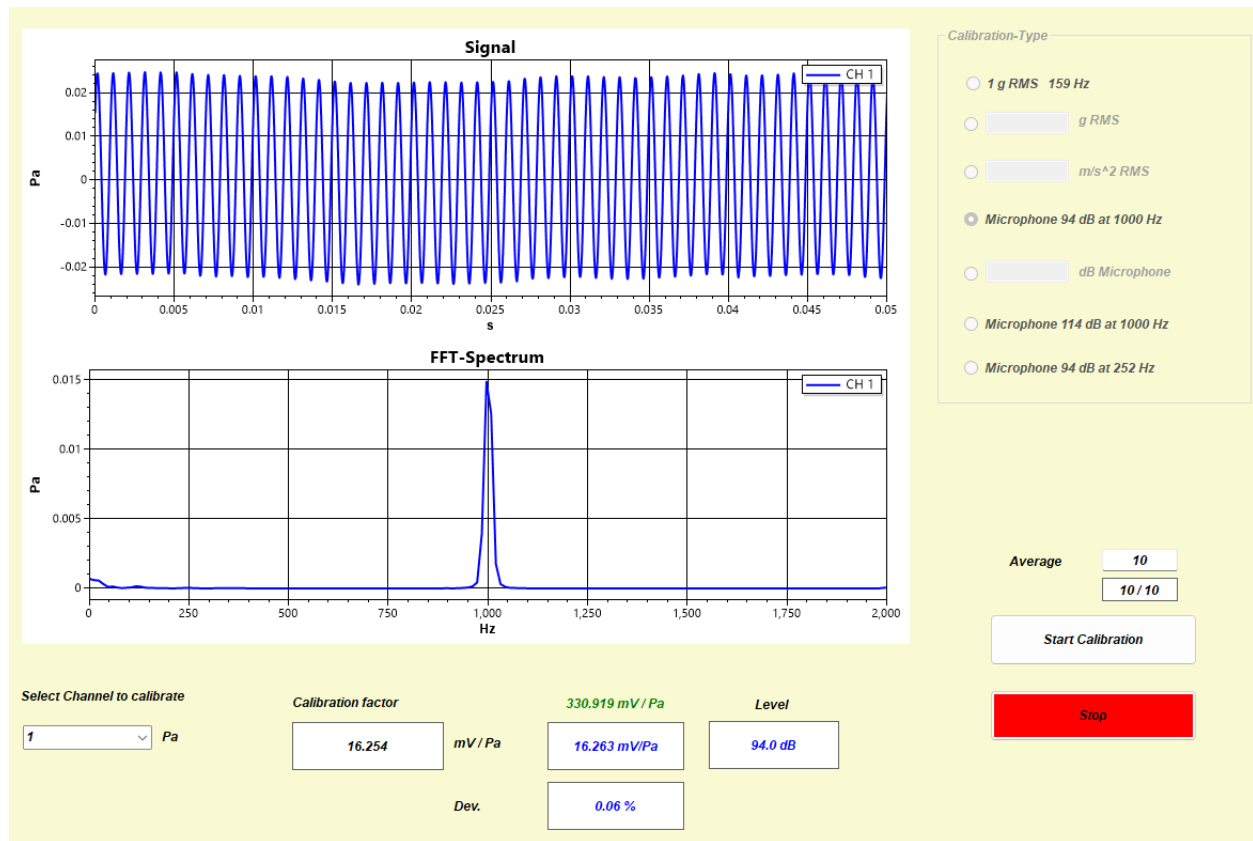
Figure 43: Calibration of the ultrasonic microphone at 94 dB at 1000 Hz.
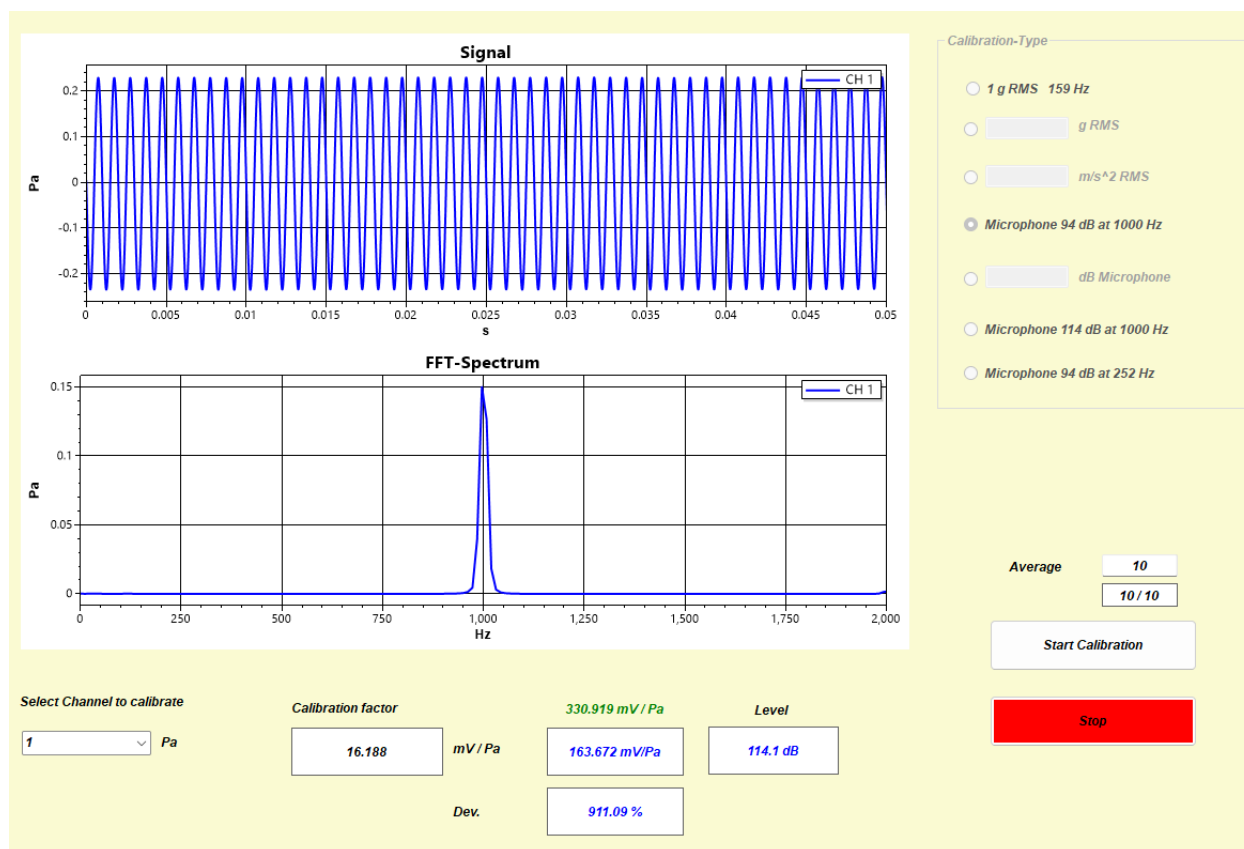
Figure 44: Calibration test at 114 dB.
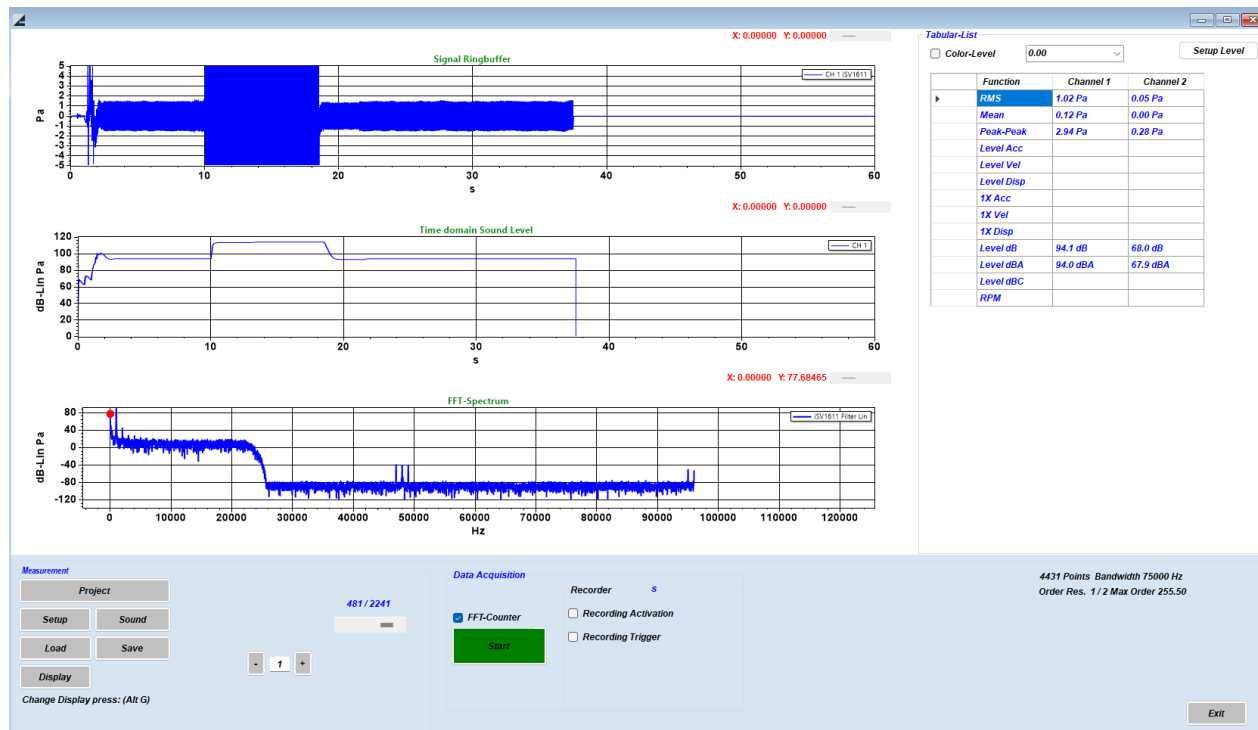
Figure 45: Result of switching between 94 dB and 114 dB.

The microphone from Roga Instruments included a calibrator, making calibration an easy task. The results of calibration are in the above figures, and the general spectra generated during a measurement is shown in figure 45. The important spectra to focus on is the middle and bottom ones, the sound level (dB) and fast Fourier transform (FFT). Looking at the dB vs. time spectrum in the middle, the signal rising to the 94 dB can be seen with a quick rise time of about 1 second. It then stabilizes at 94 dB, and when the 114 dB button is pressed around 10 seconds, the signal immediately jumps to that level. Using an ultrasonic noise emitter app, readings at 2 kHz, 5 kHz, 10 kHz, and 15 kHz were taken. The frequency range of this microphone ends at 20 kHz, so readings above 15 kHz were difficult to see in the spectrum.
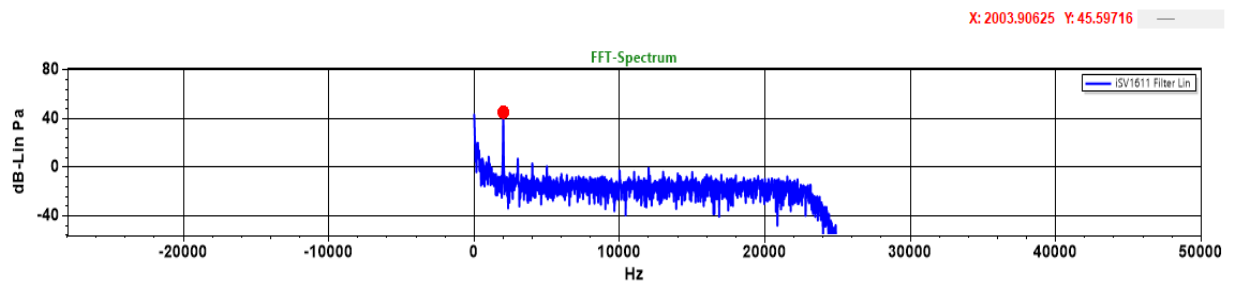
Figure 46: FFT Spectrum at 2 kHz.
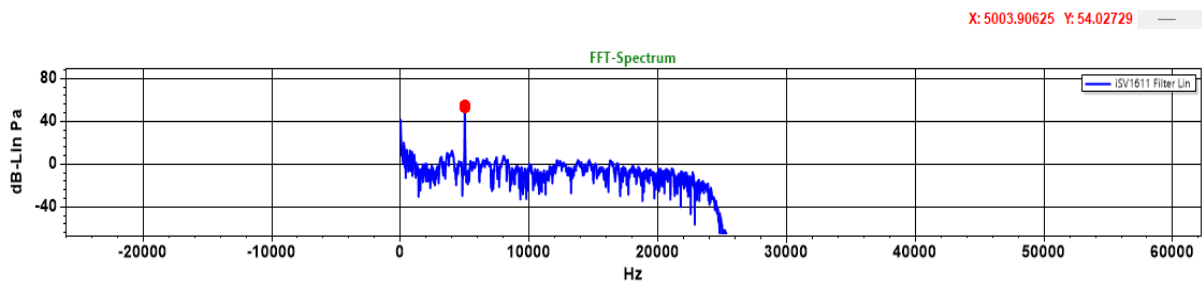
Figure 47: FFT Spectrum at 5 kHz.
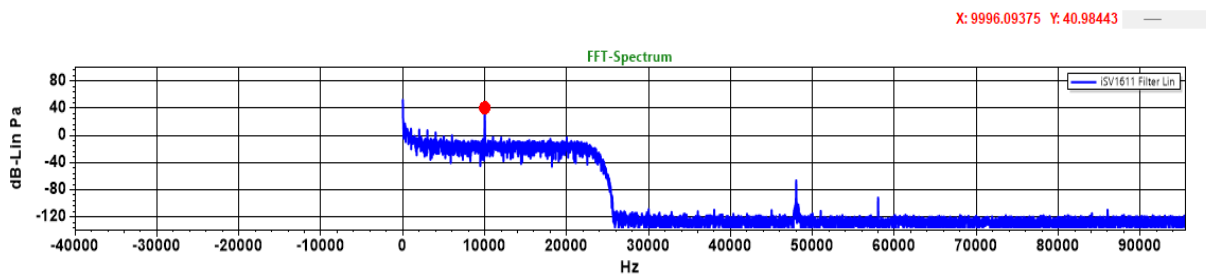
Figure 48: FFT Spectrum at 10 kHz.
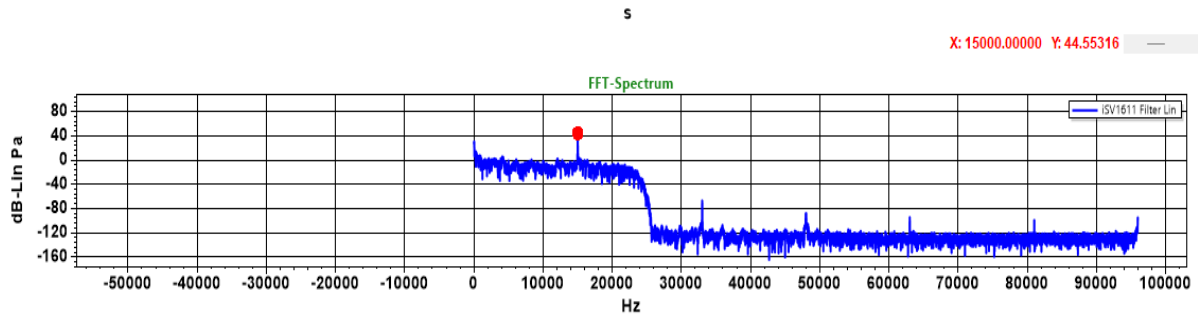
Figure 49: FFT Spectrum at 15 kHz.

As seen in each FFT spectrum, the microphone read each signal at either exactly the frequency being emitted or within 4 Hz, a negligible error. These readings are seen at the placed red dot in each spectrum and in the "x" value in the top right. The spectra for 10 and 15 kHz was expanded to show more to show the FFT phenomena of frequencies added together. In each spectrum the sampling rate, or number of audio samples taken per second, was set to 192 kHz. This sampling rate was chosen so the largest spectrum would appear. There are, however, more peaks in the spectra. Though the range of the microphone is 20 kHz, the higher frequencies seen in the spectrum are at a level of almost silence down at -100 dB. A 48 kHz peak exists for an unknown reason, but the most likely explanation is an electronic emitting this frequency at an extremely low sound level or an internal signal being picked up. In figure 48, the 10 kHz spectrum, there is a peak at 58 kHz, representing the 48 kHz and 10 kHz frequencies added together. This is also seen in figure 49, where there is a peak at 63 kHz, representing 48 kHz and 15 kHz added together. However, there is also a peak at 33 kHz, representing 15 kHz subtracted from 48 kHz, showing the "mirror" characteristic of a FFT spectrum.

In addition to the noise tests, an eyeball test was done to see if distance has an effect. The eyeball test answered no to that, as when the microphone was moved many feet away from the frequency emission source, the peaks maintained their amplitude. This observation is important because when measuring for higher frequency sounds for potential leaks, the microphone will still pick up the noise from a far distance.

CHAPTER 5 – CONCLUSIONS AND FUTURE WORK

5.1 Conclusions

The data obtained from the experiments completed for this work were sufficient in providing the desired outcomes. The characterization of a Kromek CZT gamma spectrometer, a FLIR Duo-R thermal camera, and a Roga Instruments ultrasonic microphone was successfully completed showing that this system of devices could be used to detect leaks from the HLW storage tanks at SRS and HS via three leak's signatures: a gamma ray signature, a heat signature, and a sound signature.

The Kromek CZT detector measured a 0.898 µCi (as of today 0.675 µCi due to half-life decay) and 16 µCi (now 11.94 µCi due to half-life decay) sealed ^{137}Cs source. These were referred to by their original activity levels for simplicity's sake. As ^{137}Cs is the primary γ-ray emitter problem in the HLW tanks, using the same isotope is advantageous for accurate results to be applied to the field. Gamma-ray spectra were generated through the KSpect software and the gaussian distributions were analyzed for accuracy. Measurements were taken from different distances, and while measurements from further away were less accurate, the largest error in measurement was only 0.244%, meaning the detector is very accurate. Even with a slight deviation, a scientist or engineer would still be able to identify the isotope as ^{137}Cs. The most accurate reading was from the 16 µCi source measured flush against it with an error of 0.01%. Additionally, all the measurements had energy resolutions close to or below the given 2.5%, giving more of an indication of the accuracy of the device and measurements.

The FLIR Duo-R thermal camera was used to image different shapes of metal objects against an ambient temperature background. The metal objects used were a small rod, a ruler, a

ring, and a plate. These different shapes were used to show how the camera can detect hot spots of various sizes and shapes in the field. Addiionally, the heat distribution through the table from the heated objects was observed, showing how heat would move through the walls of the tank if a leak were to occur in the field. Through some innovation to reduce reflection problems and cooling problems, the objects were successfully imaged and easily identified in the thermal images. The color contrast between red/orange (hot) and blue (cold) allowed for easy observation of the hot spots. In addition, the color contrast was elevated more when the temperature variation was higher. This successfully shows that in the field, if there is a leak in a tank where high heat is being emitted due to ^{90}Sr, a thermal camera would readily distinguish a hot spot several degrees higher than the ambient in the environment.

Finally, a Roga Instruments iSV1611USB microphone was used to test ultrasonics. A leak in a pressurized vessel such as the HLW tanks would emit a high frequency noise, potentially higher than the human ear could hear, especially with machinery and electronics whirring in the background. The microphone had a frequency range up to 100 kHz, but emissions of 2 kHz, 5 kHz, 10 kHz, and 15 kHz were measured due to lack of availability of a high frequency noise. The microphone was able to hear these emissions from many feet away and generate a peak in the FFT spectrum with almost zero error. The accuracy and ability to display the frequency on the spectrum shows how the microphone would be useful in the field finding a leak.

5.2 Future Work

Something to look at in future work to build on this work [71] is exploring using either different or additional devices when detecting each signature. Gamma-ray detection could be measured utilizing larger CZT detectors or even scintillators such as sodium-iodide (NaI). Larger thermal cameras with higher resolution and better accuracy can be experimented with to explore

whether the better accuracy is necessary in this application. Multiples of the devices used in this work could also be tested at the same time, for example utilizing multiple CZT detectors at different angles or material blockers to emulate a drone or robot moving around a HLW tank. Multiple thermal cameras could be utilized at once to view heated objects from different points of view and distances, as well as measure multiple objects at once.

The other focus of future work would be conducting the larger scale experimentation, then move to automation and field application. Due to the nature of the rules regarding radiation, only small, sealed sources could be used in the lab on campus. Additionally, they could not be removed from the lab. Future work could involve sources in an outdoor setting in various geometries to test the gamma detector. Additional study in larger scale heated objects or pipes for the thermal camera and ultrasonic microphone, respectively, would allow for more readings to verify accuracy at higher temperatures and sound frequencies.

Utilizing drone and robot technology would allow for these devices to be integrated into either a flying drone or a ground platform (e.g., a walking robot). Integration into a drone alongside a Wi-Fi signal and GPS would allow for not only the detection of a leak, but also the location. Proving the system of leak detection devices can be simultaneously used on a remotely operated mechanism would be essential in the progress towards utilizing this technology in the tank farms at SRS and HS.

APPENDIX

Device Specifications

Kromek Gamma-ray Spectrometer

Specification (GR1 and GR1-A)   CE

Detector	10mm x 10mm x 10mm CZT detector
Energy range	30 keV to 3.0 MeV
Energy resolution	<2.5% FWHM @ 662 keV
Electronic noise	<10 keV FWHM
Maximum throughput	30,000 counts/s
Number of channels	4096 (12 bit)
Differential non-linearity	< ± 1%
Power consumption	250 mW
Dimensions	25mm x 25mm x 63mm
Weight	60 gram
Temperature	0 - 40°C

[66] *Gr family*. Kromek. (2023, May 4). https://www.kromek.com/product/gr-family/

FLIR Duo-R Thermal Camera

Specifications

Overview	FLIR Duo R
Thermal Imager	Uncooled VOx Microbolometer
Sensor Resolution	160 × 120
Lens	57° × 44°
Spectral Band	7.5 – 13.5 μm
Thermal Frame Rates	7.5 Hz (NTSC); 8.3 Hz (PAL)
Thermal Measurement Accuracy	+/-5°C
Visible Camera Resolution	1920 × 1080
Visible Camera FOV	90°
Physical Attributes	
Size	41 × 59 × 29.6 mm
Weight	84 grams
Image Processing & Display Controls	
Image Optimization for sUAS?	Yes
Multiple Color Palettes?	Yes – Adjustable in App and via PWM
MSX Enhancement?	Yes
Picture-in-Picture?	Yes
Interfacing	
Mini-USB Connector	Power in, Analog video out, PWM connections, MAVLink control
Input Voltage	5.0 - 26.0 VDC
Power Dissipation (Peak)	2.2 W (3.3 W)
Remote Control	Two PWM Controls (assigned in App)
MAVLink interface?	Yes
Digital Video Output	Micro-HDMI; HDMI video at 1080p
Storage Media	Micro-SD card
Environmental	
Operating Temperature Range	0°C to +50°C
Storage Temperature Range	-20°C to +60°C
Operational Altitude	+12,000 feet

[67] FLIR. (n.d.). *Duo-R-Datasheet-US.* [Data sheet].

Roga Instruments iSV1611 USB Microphone
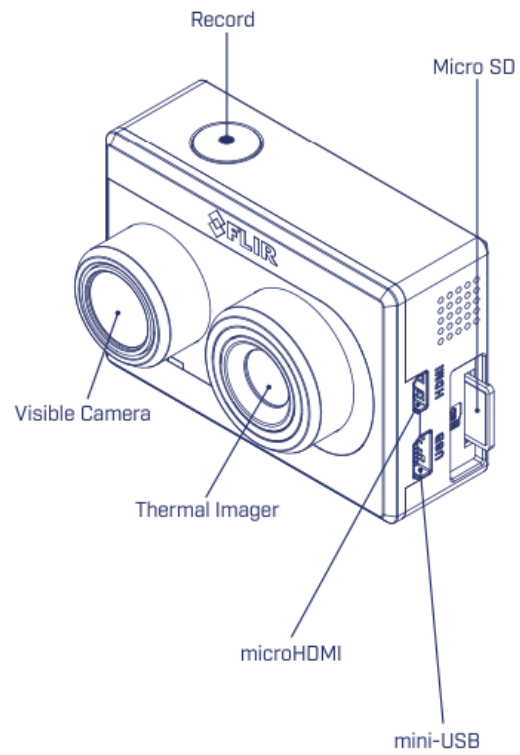
Technical data

A/D sampling frequency kHz	48/96/192
Frequency range (+/- 1.5 dB)	5 Hz - 80 kHz
Microphone capsule thread	60US
Polar pattern	Sphere
Electrical noise floor	12 dB (A)
Acoustic background noise	35 dB (A)
Limit sound pressure level	158dB
Sensitivity	3.5 mV/Pa
Measuring range	35dBA − 158 dB
USB Standard	2.0 & 1.1
Dimensions mm	φ20×230 mm
1/4" outsidediameter	7.0 ± 0.02 mm
Weight	125 g

[72] Roga Instruments. *iSV1611 Ultra Microphone.* User manual. https://roga-instruments.com/downloads/PDF/iSV1611-Ultra-EN.pdf

REFERENCES

[1] The Hanford Site. (2022). *Hanford Tank Farms* [Fact Sheet]. U.S. Department of Energy. https://www.hanford.gov/files.cfm/Tank_Farm_Overview_Fact_Sheet_Nov20221.pdf

[2] Savannah River Site. (2021). *Liquid Waste Tank Farms* [Fact Sheet]. U.S. Department of Energy. https://www.srs.gov/general/news/factsheets/srr_radioactive_tank_farms.pdf

[3] Evaluation of Criteria for Selecting a Salt Processing Alternative for High Level Waste at the Savannah River Site: Interim Report. (2001). In *National Academies Press eBooks*. https://nap.nationalacademies.org/read/10088/chapter/12

[4] U.S. Environmental Protection Agency. (n.d.). *EPA Facts about Strontium-90* [Fact Sheet]. https://semspub.epa.gov/work/HQ/175430.pdf

[5] U.S. Environmental Protection Agency. (n.d.). *EPA Facts about Cesium-137* [Fact Sheet]. https://semspub.epa.gov/work/HQ/176309.pdf

[6] M. Arguelles Perez, W. Yim, A. Barzilov, "CZT Sensor Based Radiation Source Localization Using Multiple Autonomous UAVs," *Waste Management Symposia* (WM-2023), Phoenix, AZ, February 26 - March 2, 2023.

[7] Barzilov, A., Kazemeini, M., "Unmanned Aerial System Integrated Sensor for Remote Gamma and Neutron Monitoring," *Sensors* 20, 5529 (2020).

[8] Yim, W., Cook, A., Kazemeini, M., Barzilov, A., "Low-Altitude Contour Mapping of Radiation Fields Using UAS Swarm," *Intelligent Service Robotics* 12, 219 (2019).

[9] Kazemeini, M., Barzilov, A., Yim, W., Lee, J., "Gamma Ray and Neutron Sensors for Remote Monitoring using Aerial Platforms," *Sensors and Transducers* 229, 47 (2019).

[10] Kazemeini, M., Cook, Z., Lee, J., Barzilov, A., Yim, W., "Plug-and-Play Radiation Sensor Components for Unmanned Aerial System Platform," *Journal of Radioanalytical and Nuclear Chemistry* 318, 1797 (2018).

[11] Kazemeini, M., Barzilov, A., Lee, J., Yim, W., "Integration of CZT and CLYC radiation detectors into robotic platforms using ROS," *AIP Conf. Proc.* 2160, 050019 (2019).

[12] Kazemeini, M., Barzilov, A., "Dual-Mode Radiation Sensor for UAS Platforms," *Proceedings* 42, 37 (2020).

[13] Kazemeini, M., Barzilov, A., Vargas, J., Yim, W., Novikov, I., "MLE Localization of Radiation Sources in Aerial Remote Sensing," *International Congress on Advances in Nuclear Power Plants* (ICAPP-2019), Juan-les-Pins, France, May 12-15, 2019.

[14] Kazemeini, M., Vazquez, G., Barzilov, A., Yim, W., "UAS Based Remote Sensing for

Nuclear Power Plants," *International Congress on Advances in Nuclear Power Plants* (ICAPP-2019), Juan-les-Pins, France, May 12-15, 2019.

[15] Lee, J., Hartman, J., Cook, Z., Lee, J.S., Yim, W., Barzilov, A., "Development of Plug-and-Play Interchangeable Components for Unmanned Aerial System with Mobile Manipulation Capability," *Transactions of American Nuclear Society* 115 (2016).

[16] Kazemeini, M., Vargas, J., Barzilov, A., Yim, W., "Gamma-Ray Measurements Using Unmanned Aerial Systems," Chapter in the book *Gamma Rays*, Ed., IntechOpen, London, United Kingdom (2019). DOI: 10.5772/intechopen.82798.

[17] A. Barzilov, J. Hartman, I. Novikov, "Remote Sensing of Neutron and Gamma Radiation using Unmanned Aerial System," *Proc. IEEE* Nuclear Sci. Symp., San Diego, CA (2015).

[18] *The Actinide Research Quarterly: 2nd Quarter 2002*. (2002). Retrieved January 24, 2024, from https://www.lanl.gov/orgs/nmt/nmtdo/AQarchive/02fallwinter/NDA.html

[19] *How Do Thermal Cameras Work?* (2020). https://www.flir.com/discover/rd-science/how-do-thermal-cameras-work/

[20] Purves D, Augustine GJ, Fitzpatrick D, et al., editors. Neuroscience. 2nd edition. Sunderland (MA): Sinauer Associates; 2001. *The Audible Spectrum*. Available from: https://www.ncbi.nlm.nih.gov/books/NBK10924/

[21] U.S. Department of Energy. (n.d.). *Manhattan project background information and preservation work*. Energy.gov. https://www.energy.gov/lm/manhattan-project-background-information-and-preservation-work

[22] Edgemon, G. L., Anda, V. S., Berman, H. S., Johnson, M. E., & Boomer, K. D. (2009). History and operation of the Hanford high-level waste storage tanks. *CORROSION*, *65*(3), 163–174. https://doi.org/10.5006/1.3319125

[23] Wiersma, B. J. (2014). The performance of Underground Radioactive Waste Storage Tanks at the Savannah River Site: A 60-year historical perspective. *JOM*, *66*(3), 471–490. https://doi.org/10.1007/s11837-014-0870-x

[24] *Hanford Overview*. Hanford overview - Washington State Department of Ecology. (n.d.). https://ecology.wa.gov/waste-toxics/nuclear-waste/hanford-cleanup/hanford overview#:~:text=Today%2C%20there%20are%20177%20underground,of%20decades%20of%20plutonium%20production.

[25] *Plutonium Manufacture and Fabrication*. The Nuclear Weapon Archive. (n.d.). https://nuclearweaponarchive.org/Library/Plutonium/index.html

[26] National Center for Biotechnology Information (2024). PubChem Element Summary for Atomic Number 92, Uranium. Retrieved January 25, 2024

from https://pubchem.ncbi.nlm.nih.gov/element/Uranium.

[27] *Half-life (radiological)*. NRC Web. (n.d.).
   https://www.nrc.gov/reading-rm/basic-ref/glossary/half-life-radiological.html

[28] Plutonium fact sheet - HPS chapters. (2001).
   http://hpschapters.org/northcarolina/NSDS/neptunium.pdf

[29] *Washington and Doe Reach an agreement on leaking Hanford Tanks*. ANS. (2022, August
   26).   https://www.ans.org/news/article-4264/washington-and-doe-reach-an-agreement-on-
   leaking-hanford-tanks/#:~:text=In%20April%202021%2C%20following%20a%20year-
   long%20leak%20assessment%2C,a%20gallon%20a%20day%2C%20according%20to%20t
   he%20DOE

[30] Lini, D. C. (1975). *Compilation of Hanford Corrosion Studies*. Compilation of Hanford
   corrosion studies (Technical Report) | OSTI.GOV. https://www.osti.gov/biblio/4165497/

[31] Engineering Department | Arc Machines, Inc. (2023, July 24). *Welding stress corrosion
   cracking: Understanding the hidden threat*. Arc Machines.
   https://resources.arcmachines.com/welding-stress-corrosion-cracking-understanding-the-
   hidden-threat-
   ami/#:~:text=The%20expansion%20and%20contraction%20of,these%20systems%20conta
   in%20are%20corrosive.

[32] Wiersma, B. J. (2008). An Assessment of the Service History and Corrosion Susceptibility
   of Type IV Waste Tanks. *Savannah River National Laboratory Materials Science and
   Technology Directorate.*
   https://digital.library.unt.edu/ark:/67531/metadc894981/m2/1/high_res_d/939191.pdf

[33] International Atomic Energy Agency. (n.d.). Livechart - table of nuclides - nuclear structure
   and decay data. https://www-nds.iaea.org/relnsd/vcharthtml/VChartHTML.html

[34] United States Nuclear Regulatory Commission. (n.d.). *What are the different types of
   radiation?*. NRC Web. https://www.nrc.gov/reading-rm/basic-ref/students/science-
   101/what-are-different-types-of-radiation.html

[35] Murray, R. L. (1981). *Understanding Radioactive Waste.* U.S. Department of Energy,
   Pacific Northwest Laboratory.
   https://inis.iaea.org/collection/NCLCollectionStore/_Public/14/725/14725278.pdf

[36] U.S. Department of Energy. (n.d.). *Alpha particles*. Manhattan Project: Science >
   Radioactivity > ALPHA PARTICLES. https://www.osti.gov/opennet/manhattan-project-
   history/Science/Radioactivity/alpha.html

[37] *Beta particle*. NRC Web. (n.d.). https://www.nrc.gov/reading-rm/basic-ref/glossary/beta-particle.html#:~:text=A%20negatively%20charged%20beta%20particle,if%20they%20enter%20the%20body

[38] Heilbronn, Lawrence. (2015). Neutron Properties and Definitions [supplemental material]. National Aeronautics and Space Administration. https://three.jsc.nasa.gov/articles/Heilbronn_Neutron_Supplement.pdf

[39] Shampo, M. A., Kyle, R. A., & Steensma, D. P. (2011). Hans Geiger—German physicist and the Geiger Counter. *Mayo Clinic Proceedings*, *86*(12). https://doi.org/10.4065/mcp.2011.0638

[40] P. Guss, T. G. Stampahar, S. Mukhopadhyay, A. Barzilov, and A. Guckes, "Scintillation properties of a $Cs_2LiLa(Br_6)90\%(Cl_6)10\%$:Ce (CLLBC) crystal," SPIE Proceedings, 2014. doi:10.1117/12.2060204

[41] A. Pour Yazdanpanah, et al., "Sparse-View Neutron-Photon Computed Tomography: Object Reconstruction and Material Discrimination," *Applied Radiation and Isotopes* 132, 122-128 (2018).

[42] J. Hartman, A. Barzilov, "Combined Photon-Neutron Radiography for Nondestructive Analysis of Materials," *Journal of Radioanalytical and Nuclear Chemistry* 307, 2307-2312 (2016).

[43] J. Hartman, et al., "3D Imaging using Combined Neutron-Photon Fan-Beam Tomography: a Monte Carlo Study," *Applied Radiation and Isotopes* 111, 110-116 (2016).

[44] J. Hartman, A. Barzilov, "Computational Study of Integrated Neutron/Photon Imaging for Illicit Material Detection," *Physics Procedia* 66, 85 (2015).

[45] A. Barzilov, B. Kessler, P. Womble, "Analysis of 14-MeV Neutron Induced Gamma-Ray Spectra using Multiwavelets," *Radiation Measurements* 79, 43 (2015).

[46] A. Barzilov, P. Womble, "Study of Doppler Broadening of Gamma-Ray Spectra in 14-MeV Neutron Activation Analysis," *Journal of Radioanalytical and Nuclear Chemistry* 301, 811 (2014).

[47] A. Barzilov, I. Novikov, B. Cooper, "Computational Study of Pulsed Neutron Induced Activation Analysis of Cargo," *Journal of Radioanalytical and Nuclear Chemistry* 282, 177 (2009).

[48] A. Barzilov, I. Novikov, P. Womble, "Material Analysis Using Characteristic Gamma Rays Induced by Pulse Neutrons," Chapter in *Gamma Radiation*, pp.17-40, Ed. F. Adrovic, Intech, ISBN 979-953-307-361-2 (2012).

[49] J. Hartman, A. Barzilov, E. Peters, S. Yates, "Measurements of Response Functions of EJ

299-33A Plastic Scintillator for Fast Neutrons," *Nuclear Instruments and Methods in Physics Research A* 804, 137-143 (2015).

[50] J. Hartman, A. Barzilov, "Development of a Phoswich Neutron Detector with Energy Spectroscopy Capability," *Transactions of American Nuclear Society* 114, 958 (2016).

[51] *About pmts: Photomultiplier Tubes (pmts)*. Hamamatsu Photonics. (n.d.). https://www.hamamatsu.com/us/en/product/optical-sensors/pmt/about_pmts.html

[52] *Scintillations Materials Research Center*. Tickle College of Engineering. (2022, July 20). https://tickle.utk.edu/smrc/

[53] N. D'Olympia *et al.*, "Pulse-shape analysis of CLYC for thermal neutrons, fast neutrons, and gamma-rays," *Nuclear Instruments and Methods in Physics Research Section A: Accelerators, Spectrometers, Detectors and Associated Equipment*, vol. 714, pp. 121–127, 2013. doi:10.1016/j.nima.2013.02.043

[54] N. D'Olympia, P. Chowdhury, E. G. Jackson, and C. J. Lister, "Fast neutron response of ^{6}Li-depleted CLYC detectors up to 20 MeV," *Nuclear Instruments and Methods in Physics Research Section A: Accelerators, Spectrometers, Detectors and Associated Equipment*, vol. 763, pp. 433–441, 2014. doi:10.1016/j.nima.2014.06.074

[55] D. Pérez-Loureiro *et al.*, "Evaluation of CLYC-6 and CLYC-7 scintillators for detection of nuclear materials," *Nuclear Instruments and Methods in Physics Research Section A: Accelerators, Spectrometers, Detectors and Associated Equipment*, vol. 1012, p. 165622, 2021. doi:10.1016/j.nima.2021.165622

[56] J. Qin *et al.*, "Characteristic of a $Cs_2LiLaBr_6$:Ce scintillator detector and the responses for fast neutrons," *Nuclear Instruments and Methods in Physics Research Section A: Accelerators, Spectrometers, Detectors and Associated Equipment*, vol. 905, pp. 112–118, 2018. doi:10.1016/j.nima.2018.05.006

[57] A. Guckes, A. Barzilov, P. Guss, "Experimental Study of Directional Detection of Neutron and Gamma Rays Using an Elpasolite Scintillator Array," *Nuclear Instruments and Methods in Physics Research A* 992, 165028 (2021).

[58] A. Guckes, A. Barzilov, P. Guss, "Directional Detection of Neutrons and Photons Using Elpasolites: Computational Study," *Radiation Measurements* 124, 127-131 (2019).

[59] A. Barzilov, A. Guckes, "Time Encoded Imaging of Neutrons and Photons Using CLYC Detector Equipped with a Dual Mode Collimator," *Sensors & Transducers* 229(1), 78-83 (2019).

[60] A. Guckes, A. Barzilov, "Development and Deployment of the Collimated Directional Radiation Detection System," *Proc. SPIE* 10393, Radiation Detectors in Medicine, Industry, and National Security XVIII, 1039306 (2017).

[61] P. Guss, T. Stampahar, S. Mukhopadhyay, A. Barzilov, A. Guckes, "Maximum Likelihood Source Localization Using Elpasolite Crystals as a Dual Gamma-Neutron Directional Detector," *Proc. SPIE* 9595: Radiation Detectors: Systems and Applications XVI, 959502 (2015).

[62] Venkataraman, R. (2020). Semiconductor detectors. In *Handbook of Radioactivity Analysis* (pp. 409–491). Elsevier Science & Technology. https://doi.org/10.1016/B978-0-12-814397-1.00004-2

[63] *What is a wide-band-gap semiconductor?*. What is a wide-band-gap semiconductor? | Toshiba Electronic Devices & Storage Corporation | Americas – United States. (n.d.). https://toshiba.semicon-storage.com/us/semiconductor/knowledge/faq/diode_sic-sbd/sic-sbd001.html

[64] *Electron Hole*. Electron hole - Energy Education. (n.d.). https://energyeducation.ca/encyclopedia/Electron_hole

[65] Quam, William. Cadium-Zinc-Telluride (CZT) Gamma Ray Spectrometry. United States. https://doi.org/10.2172/788884

[66] *GR family*. Kromek. (2023, May 4). https://www.kromek.com/product/gr-family/

[67] FLIR. (n.d.). *Duo-R-Datasheet-US.* [Data sheet].

[68] C. Towles, J. Clarke, J. Batista, H. Frey, J. Moon, A. Barzilov, A. Okeani, "Absorption Capabilities of Zeolite and Zero Valent Iron with High-Level Waste Tank Radionuclides and Metals: Cesium, Strontium and Chromium," *Waste Management Symposia* (WM-2024), Phoenix, AZ, March 10-14, 2024.

[69] J. Clarke, C. Towles, H. Frey, A. Okeani, J. Batista, J. Moon, A. Barzilov, "Efficient Sorbent Wattle Design for High- Level Nuclear Waste Tanks," *Waste Management Symposia* (WM-2024), Phoenix, AZ, March 10-14, 2024.

[70] A. Barzilov, J. Clarke, H. Frey, A. Okeani, C. Towles, J. Wolfe, J. Moon, J. Batista, "Active Barrier to Capture Releases of Chromium, Cesium and Strontium from Leaking Waste Tanks," *Waste Management Symposia* (WM-2024), Phoenix, AZ, March 10-14, 2024.

[71] H. Frey, A. Okeani, J. Clarke, J. Batista, J. Moon, A. Barzilov, J. Wolfe, C. Towles, "Remote Detection of leaks in HLW Storage Tanks," *Waste Management Symposia* (WM-2024), Phoenix, AZ, March 10-14, 2024.

[72] Roga Instruments. *iSV1611 Ultra Microphone.* User manual. https://rogainstruments.com/downloads/PDF/iSV1611-Ultra-EN.pdf

CURRICULUM VITAE

Hunter Frey

Hfrey1999@hotmail.com

Degree obtained:

Bachelor of Science, Mechanical Engineering, December 2022

University of Nevada Las Vegas

Master's Thesis:

Remote Detection of Leaks in High Level Waste Storage Tanks

Thesis Committee Members:

Dr. Alexander Barzilov, Committee Chair

Dr. Jeremy Cho, Committee Member

Dr. Charlotta Sanders, Committee Member

Dr. Emma Regentova, Graduate College Representative